Galvanic Replacement and Etching of MAX-Related Phases in Molten Salts toward MXenes: An In Situ Study

Emile Defoy, Marzena Baron, Amandine Séné, Anissa Ghoridi, Dominique Thiaudière, Stéphane Célérier, Patrick Chartier, Florian Brette, Vincent Mauchamp, David Portehault

Galvanic replacement and etching of MAX-related phases in molten salts towards MXenes: an *in situ* study

Emile Defoy,[a] Marzena Baron,[a] Amandine Séné,[a] Anissa Ghoridi,[a] Dominique Thiaudière,[b] Stéphane Célérier,[c] Patrick Chartier,[d] Florian Brette,[d] Vincent Mauchamp,[d] David Portehault[a,*]

[a] Sorbonne Université, CNRS, Laboratoire de Chimie de la Matière Condensée de Paris (CMCP), 4 place Jussieu, F-75005, Paris, France

[b] Synchrotron SOLEIL, L'Orme des Merisiers, Saint-Aubin, 91191 Gif-sur-Yvette, France

[c] Université de Poitiers, CNRS, Institut de Chimie des Milieux et Matériaux de Poitiers (IC2MP), F-86073 Poitiers, France

[d] Institute Pprime, UPR 3346 CNRS, ISAE-ENSMA, Université de Poitiers, BP 30179, 86962 Cedex Futuroscope-Chasseneuil, France

Corresponding author: david.portehault@sorbonne-universite.fr

ABSTRACT

Galvanic replacement in molten salts has recently been uncovered as a pathway to design new compositions of layered transition metal carbides related to the family of MAX phases, $M_{n+1}AlX_n$, where M is a transition metal, X is carbon for carbide phases, and A is mainly an element of IIIA and IVA groups of the periodic table. These compounds can be further involved in etching processes by removal of A elements to yield new 2D transition metal carbides $M_{n+1}X_nT_z$, so-called MXenes, where T stands for surface groups. Although promising, the chemical modification of MAX-related materials in molten salts has been reported only for few compounds and little is known about the corresponding reaction mechanisms. In this work, we question the versatility of galvanic reactions in molten salts for MAX-related phases, by combining for the first time *in situ* X-ray diffraction and *in situ* X-ray absorption spectroscopy during reactions in molten salts for two compounds: Ti_3AlC_2 and Mo_2Ga_2C. The first one shows minute-scale transformation into molten $ZnCl_2$ towards Ti_3ZnC_2, followed by evolution into $Ti_3C_2Cl_2$. On the contrary we do not observe replacement, but etching of Mo_2Ga_2C into Mo_2GaC and then orthorhombic Mo_2C, with a loss of the layered structure. We highlight the role of the molten salt chemistry in this process and discuss the different behaviors of these two MAX-related phases *versus* galvanic reactivity in molten salts, to open the way to new MAX compositions.

INTRODUCTION

MXenes are a family of 2D non-oxidic materials that exhibit important properties, especially for electrochemical energy storage, energy conversion, and for electromagnetic shielding.[1,2] The formula of MXenes is $M_{n+1}X_nT_z$ (n= 1-3), where M is a transition metal, X is carbon or nitrogen, and T represents the surface groups, which are usually derived from the synthesis process. MXenes are indeed obtained by exfoliation of $M_{n+1}AlX_n$ (MAX) phases, or other related layered compounds, where A is an oxidizable element, like aluminum, gallium or silicon.[3] The exfoliation of such compounds consists in the etching of the A element accompanied by the surface passivation with T groups, which impact the surface and properties of MXenes.[4–6] The conventional exfoliation process relies on chemical treatment in hydrofluoric acid solutions or alkaline solutions containing fluoride anions.[5] As a consequence, the termination groups are usually oxo, hydroxo or fluoride groups. Exfoliation in fluoride-based aqueous solutions then limits the versatility of the MXenes surface chemistry, and raises important environmental and safety concerns.

Other methods have been proposed to exfoliate MAX and MAX-related phases and then yield new compounds and surface termination groups.[7] Among them, reactions in molten salts are attracting interest since few years. Treatment of MAX phases in molten salts has been shown first by Urbankowski *et al.* in 2016 for etching Ti_4AlN_3 into the molten eutectic mixture of KF:NaF:LiF and form $Ti_4N_3T_z$.[8] Later, in 2019, Li *et al.* revised the approach to treat Ti_3AlC_2, Ti_2AlC, Ti_2AlN and V_2AlC into molten $ZnCl_2$ and then form new compounds: Ti_3ZnC_2, Ti_2ZnC, Ti_2ZnN, V_2ZnC, $Ti_3C_2Cl_2$, Ti_2CCl_2.[3] Few months later, Li *et al.* rationalized the underlying process, by pointing out the importance of tuning the cationic redox properties of the molten salt in respect to the redox properties of the element to be etched.[9] For instance, the authors could etch Ti_3SiC_2 by using molten $CuCl_2$. They obtained new MXenes, such as Ti_3CNT_z, Nb_2CT_z or Ta_2CT_z. At the same time, Kamysbayev *et al.* revisited the approach by treating Ti_3AlC_2 and Nb_2AlC into molten $CdBr_2/CdCl_2$ to yield $Ti_3C_2Br_z$ and Nb_2CCl_z.[6] The authors showed that the halide termination groups can be involved into further post-modifications. Liu *et al.* reported recently a similar path by treating Ti_3AlC_2 into molten $FeCl_2$.[10] The resulting $Ti_3C_2Cl_z$ phase was

further reacted into a molten Li_3N/LiCl/KCl mixture to form N-terminated groups. Finally, Baumler *et al.* have also shown that molten-salt etching is feasible with boride compounds like MoAlB,[11] although complete etching was not possible and the process was stopped at the Mo_2AlB_2 phase.

Although reactions of MAX and MAX-related phases with molten salts is becoming increasingly popular, little is known about their mechanistic pathway. Li *et al.* proposed a reaction mechanism[3] based on the identification of reaction by-products by performing X-ray diffraction (XRD) on washed powders after several reaction times. These data were in line with the intuitive pathway, involving the oxidation of interleaved A atoms by the molten salt cations, accompanied by the reduction of the latter. Once oxidized, the A components are no longer stabilized between the carbide layers and then leave the structure. They can be replaced by the reduced molten salt cations, which corresponds to a galvanic replacement reaction (**Figure 1**). Li *et al.* confirmed this interpretation.[9] If no replacement takes place, then one can qualify the process as galvanic etching (**Figure 1**).[11]

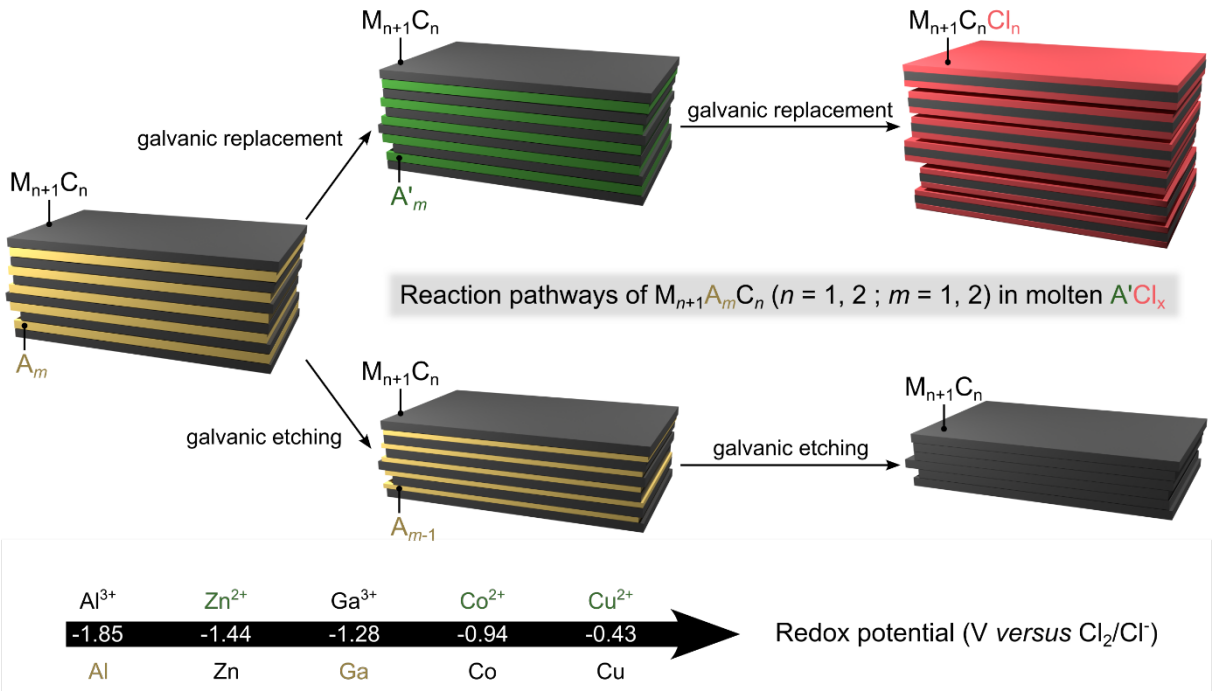

Figure 1. Scheme of galvanic reactivity of MAX-related phases in molten salts. The top branch corresponds to galvanic replacement, evidenced for Ti_3AlC_2; the bottom branch corresponds to galvanic etching, evidenced for Mo_2Ga_2C. The redox potential scale displays values from ref. [9].

Despite insightful discussions,[3,7,9] the detailed pathways of galvanic replacement and etching in

MAX and MAX-related phases are still unknown. For instance, the rate of these reactions has not been investigated and the transformation from one phase to the other has not been examined, which strongly limits the applicability of the method to new phass. Understanding these reaction paths requires both structural and chemical insights into the reaction media, which are difficult to address in molten salts: galvanic reactions of MAX and MAX-related phases occur at 400-700 °C, where it is difficult to probe reaction media *in situ*. In this context*, in situ* XRD and *in situ* X-ray absorption spectroscopy (XAS), which are sporadically used to probe molten salts,[12–15] appear as ideal techniques to study the mechanisms of galvanic reactions of MAX and MAX-related phases. The combination of *in situ* XRD and *in situ* XAS to study molten salts is however not reported to the best of our knowledge.

In this work, we thus address the mechanisms of galvanic replacement and etching of MAX-related phases by using *in situ* XRD and *in situ* XAS to probe reactions in molten salts. We provide the first insights into the coupling between redox reactivity and intercalation reactivity into MAX and MAX-related phases, by taking as case-studies the prototypal Ti_3AlC_2 MAX phase, known to undergo galvanic replacement, and the MAX-related phase Mo_2Ga_2C, known to be more refractory towards etching and whose galvanic reactions in molten salts have not been investigated.

RESULTS AND DISCUSSION

Pristine Ti_3AlC_2 and Mo_2Ga_2C powders: general *in situ* method

Ti_3AlC_2 and Mo_2Ga_2C powders have been produced by powder metallurgy and sieved to select grains size lower than 25 µm.[16,17] XRD (**Figure 2A**) indicates the sole presence of Ti_3AlC_2 and Mo_2Ga_2C as crystalline products in each powder, respectively. SEM images (**Figure 2B**) show that each powder is made of micron-scale grains.

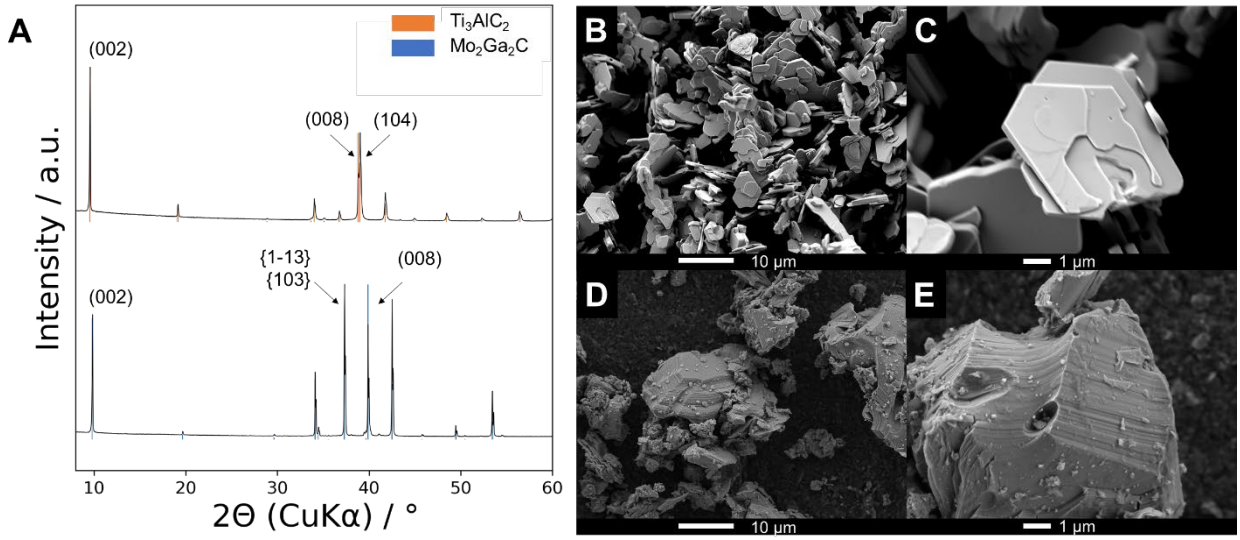

Figure 2. (A) Powder XRD patterns of the pristine products Ti_3AlC_2 and Mo_2Ga_2C, with corresponding reference patterns. SEM images of (B-C) Mo_2Ga_2C and (D-E) Ti_3AlC_2.

We discuss below *in situ* studies of the reaction of these powders into molten salts. *In situ* XRD was performed at an incident beam energy of *ca.* 18 keV, where the reaction media are sufficiently transparent to enable XRD detection in transmission mode, through a capillary. We used a capillary oven setup inspired by previous work.[12,15] To ensure homogeneity of the reaction medium, the capillary containing the reaction mixture was continuously scanned through 4 vertical positions. An XRD pattern was recorded on each position every 8.4 s with an acquisition time of 5 s. The same capillary oven used for *in situ* XRD was also used for *in situ* XAS at an energy corresponding to the K-edge of the probed element, and in fluorescence detection mode, where X-ray fluorescence was collected from the capillary at an angle of *ca.* 20 ° *versus* the incident beam, on the front side of the

oven (side of the incoming beam). Each X-ray absorption near-edge structure (XANES) required an acquisition time of 12 min. For *in situ* XAS, the capillary was not scanned but monitored on a single average position.

Galvanic reactivity of Ti_3AlC_2

We have first studied the reactivity of Ti_3AlC_2 in molten salts by focusing on the reaction designed previously by Li *et al.*,[3] in which Ti_3AlC_2 is thermally treated in molten $ZnCl_2$ (Ti_3AlC_2:$ZnCl_2$ ratio of 1:6 mol.). This reaction is a benchmark for the reactivity of a MAX phase in molten salts.

***In situ* X-ray diffraction. Figure 3A** (details in **Figures S1-S3**) shows as a heatmap the XRD patterns recorded during the reaction, by heating at 10 °C min^{-1} from room temperature to 550 °C, where we applied a temperature plateau. We identify five main stages, reported on the temperature profile in **Figure 3A**. As expected, the first one exhibits the XRD peaks of *γ*-$ZnCl_2$ and Ti_3AlC_2 and spans the range from room temperature to 280 °C. At this temperature (stage 2), *γ*-$ZnCl_2$ transforms into *δ*-$ZnCl_2$, which corresponds to the dehydration of initial *γ*-$ZnCl_2$, a structural form of $ZnCl_2$ that corresponds to a slight contamination by water traces.[18] This second temperature range lasts until 339°C, when the $ZnCl_2$-related peaks disappear, in agreement with the expected melting point. The liquid state of the reaction medium after this transition is further highlighted by a broad scattering contribution between 0.6 and 1.5 $Å^{-1}$, which is not observed at lower temperature (**Figure 3A**). The third stage occurs from the salt melting to the beginning of the 550 °C plateau and corresponds to Ti_3AlC_2 dispersed into molten $ZnCl_2$, as shown by the characteristic reflections of Ti_3AlC_2. The fourth stage starts with the temperature plateau, where we observe an abrupt shift of the MAX reflections to low *Q* values, especially the (002) and (104) peaks, which shift from 0.70 to 0.68 $Å^{-1}$ and from 2.76 to 2.73 $Å^{-1}$, respectively (**Figure 3B**). The (002) reflection corresponds to the stacking direction of Ti_3AlC_2, which indicates a change in the interleaved A species: the resulting pattern corresponds to Ti_3ZnC_2 (**Figure 3B**), which then appears as soon as the temperature plateau begins. After 24 min of plateau, we observe a new transformation,

with the appearance of a peak at 0.58 $Å^{-1}$, characteristic of the (001) reflection of $Ti_3C_2Cl_2$, as highlighted in **Figure 3B**.[3] In the course of stage (5), at 150-160 min, a transient temperature decrease was applied in order to confirm that the peak shifts were due to structural transformations and not to thermal dilatation.

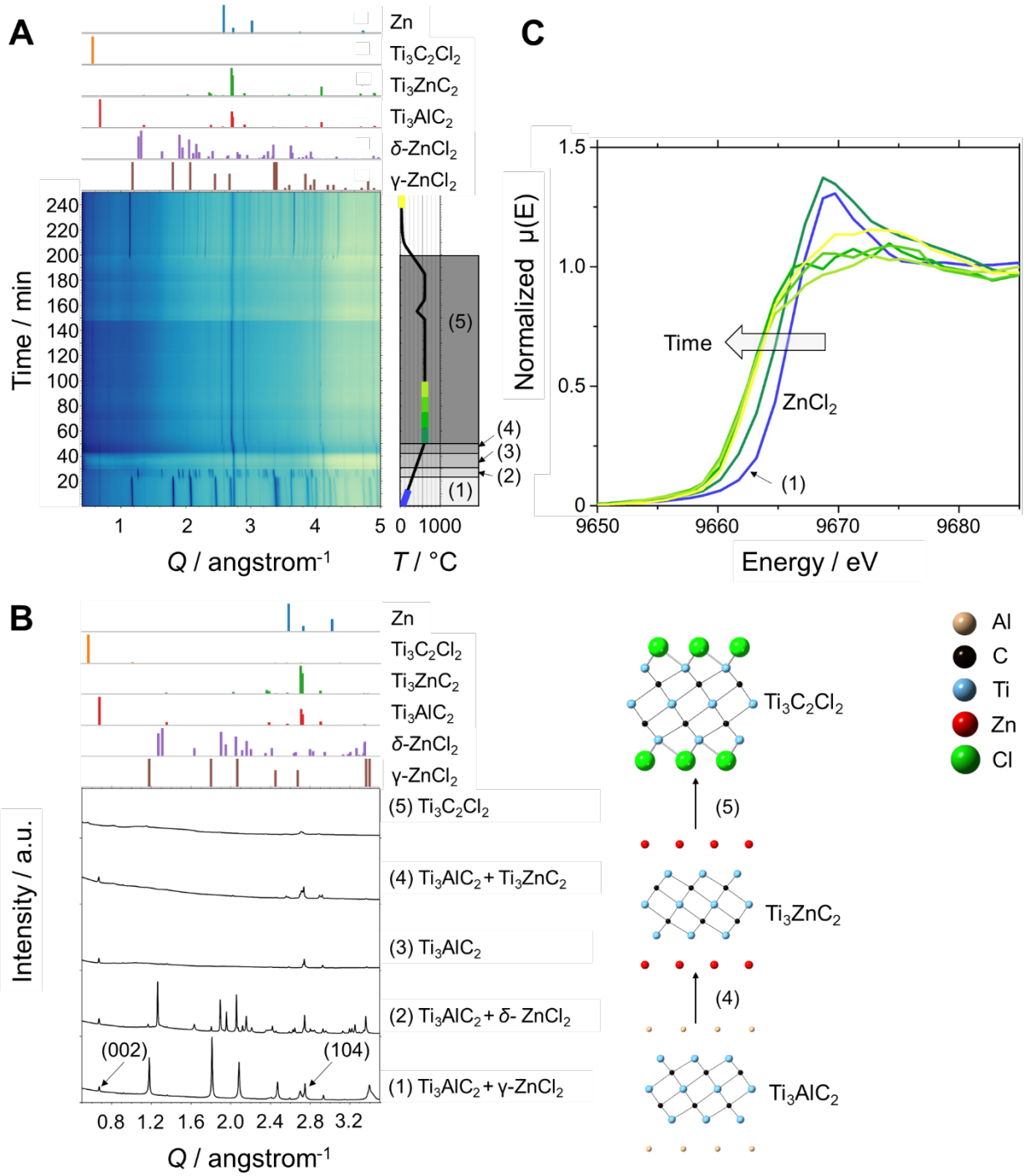

Figure 3. Galvanic reactivity of Ti_3AlC_2 into molten $ZnCl_2$. (A) *In situ* XRD patterns displayed as a heatmap; corresponding measured temperature profile on the right, and corresponding room temperature reference patterns on the top. The five stages discussed in the text are highlighted in the XRD temperature profile, with identification of the main crystalline phases. (B) XRD patterns

corresponding to selected areas of the map displayed in (A), with schemes of the crystal structures corresponding to the different temperature zones. (C) *In situ* Zn K-edge XANES recorded during a similar experiment. The time period for the acquisition of each spectrum is color-coded on the temperature profile in (A). The spectrum labelled (1) corresponds to the initial state, for which the only Zn-based component is $ZnCl_2$.

Because the transformation from Ti_3AlC_2 to Ti_3ZnC_2 seemed to occur over a surprisingly short time, on the minute-scale, we have performed *in situ* XAS at the Zn K-edge to correlate this structural transformation to chemical changes in the molten salt.

***In Situ* X-ray absorption spectroscopy.** Before the 550 °C plateau, the XANES recorded at the Zn K-edge during the reaction of Ti_3AlC_2 into molten $ZnCl_2$ (**Figure 3C**) do not show any significant modification compared to the initial state (spectrum labelled (1) $ZnCl_2$), which corresponds to the $ZnCl_2$ reference spectrum, as no reaction occurs at room temperature. When the plateau is reached, we observe a clear shift of about 3 eV of the Zn K-edge to low energy, which highlights an average decrease of the oxidation state of Zn in the melt (dark green spectrum), although the Zn K-edge energy does not reach the value reported for elemental Zn,[19] which is consistent with reduction of only a fraction of $ZnCl_2$ in large excess. This behaviour agrees with galvanic replacement of Al by Zn to form Ti_3ZnC_2, in agreement with *in situ* XRD and with the following equation:

$$Ti_3AlC_2 + 1.5\ ZnCl_2 \rightarrow Ti_3ZnC_2 + 0.5\ Zn_{(l)} + AlCl_{3\,(g)} \qquad (1)$$

The Zn K-edge shift is observed for the first XANES recorded at the beginning of the temperature plateau (brown in **Figure 3A** and **3C**), where the spectrum corresponds to a mixture of $ZnCl_2$ (in large excess), Ti_3ZnC_2 and elemental zinc formed from reaction (1). At the reaction temperature, zinc is molten (T_{fus} = 420 °C) and then cannot be detected by *in situ* XRD. The second spectrum recorded on the plateau shows an additional downward shift of the Zn K-edge energy. The acquisition period overlaps with the second structural transition to $Ti_3C_2Cl_2$, which agrees with additional reduction of Zn following equation 2:

$$Ti_3ZnC_2 + ZnCl_2 \rightarrow Ti_3C_2Cl_2 + 2\ Zn_{(l)} \quad (2)$$

This reaction corresponds to the removal of interleaved Zn atoms by oxidation of the carbide layers and also of interleaved zinc, which exhibits negative partial charge according to Bader calculations (see below). This overall redox reactions satisfies electroneutrality upon incorporation of Cl^- groups.

Galvanic replacement and etching in Ti_3AlC_2. Overall, galvanic replacement of Al by Zn (equation (1)) occurs as soon as the temperature reaches 550 °C, and over few minutes. The rate of this reaction can be better quantified by monitoring the evolution of the phase fraction between Ti_3AlC_2 and Ti_3ZnC_2, as evaluated from Rietveld refinement of the XRD patterns recorded during reaction (1) (**Figure 4**). Rietveld analysis confirms that the galvanic exchange occurs over *ca.* 12 min, in agreement with *in situ* XAS data. Besides, we did not observe a continuous shift of the interlayer distance (002) during the reaction, but rather an abrupt change from 0.70 to 0.68 $Å^{-1}$ for Ti_3AlC_2 and Ti_3ZnC_2, respectively. This suggests the absence of a solid solution between Ti_3AlC_2 and Ti_3ZnC_2, and indicates that each initial Ti_3AlC_2 grains is fully converted into Ti_3ZnC_2 within the time-resolution of our *in situ* XRD experiment (5 s acquisition time). The high rate of this galvanic exchange for micron-scale grains suggests no significant limitation of the reaction rate by atom diffusion into the interlayer space.[20] Such mechanism can be related to previous knowledge on the intercalation of organic compounds in the interlayer of clays to form hybrid lamellar compounds.[20] Indeed, the incorporation of many organic molecules between clay structural layers occurs through an 'unzipping' mechanism, where the rate limiting step is the intercalation of the first molecules, or their interaction of the layer edges, which decrease significantly the interlayer interaction and then facilitate the incorporation of next molecules.[20,21] A similar 'cascading' mechanism may explain the apparent fast rate of galvanic exchange in Ti_3AlC_2: the first Al/Zn exchange in a grain decreases the cohesion between carbide layers and the intercalated atoms,[3] which facilitates further replacement.

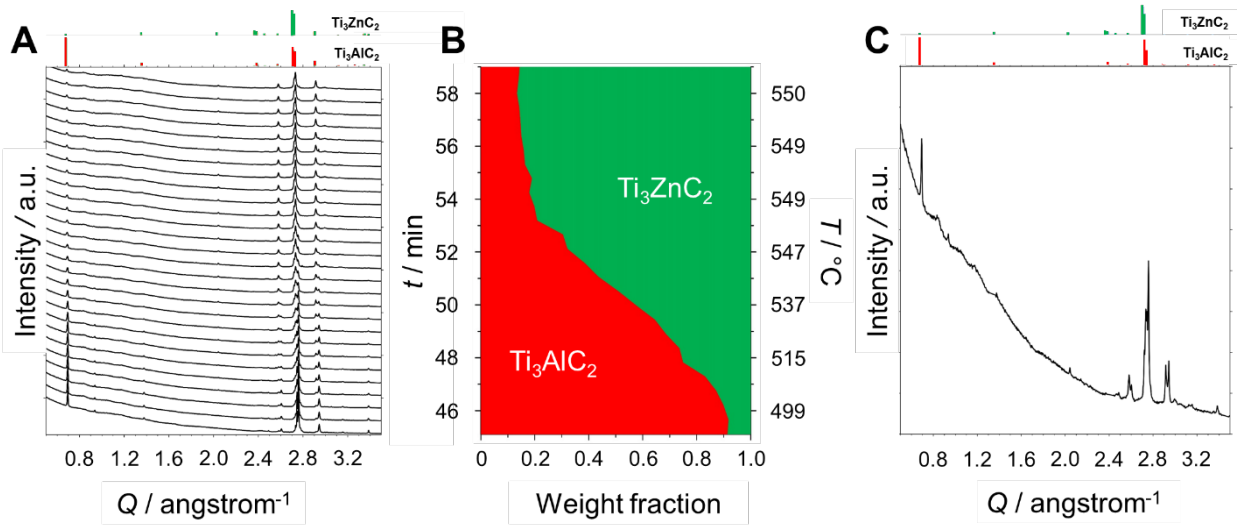

Figure 4. (A) *in situ* XRD patterns recorded during the transformation from Ti_3AlC_2 to Ti_3ZnC_2 displayed in **Figure 3**. (B) Phase fraction from sequential Rietveld refinement of the XRD patterns shown in A, with corresponding reaction time and temperature. (C) An *in situ* XRD pattern from A, showing the coexistence of Ti_3AlC_2 and Ti_3ZnC_2.

Galvanic reactivity of Mo_2Ga_2C

As a second MAX-related phase whose reactivity in molten salts has not been reported, we have studied how Mo_2Ga_2C evolves within molten salts, to assess the ability of this compound to undergo galvanic etching and/or replacement. Contrary to Ti_3AlC_2 that contains only a single layer of Al atoms, complete etching of Mo_2Ga_2C requires removal of double layers of A (Ga) atoms (**Figure 5**). Besides, Ga is more oxidant than Al, so that we expect the need for more oxidizing molten salts.

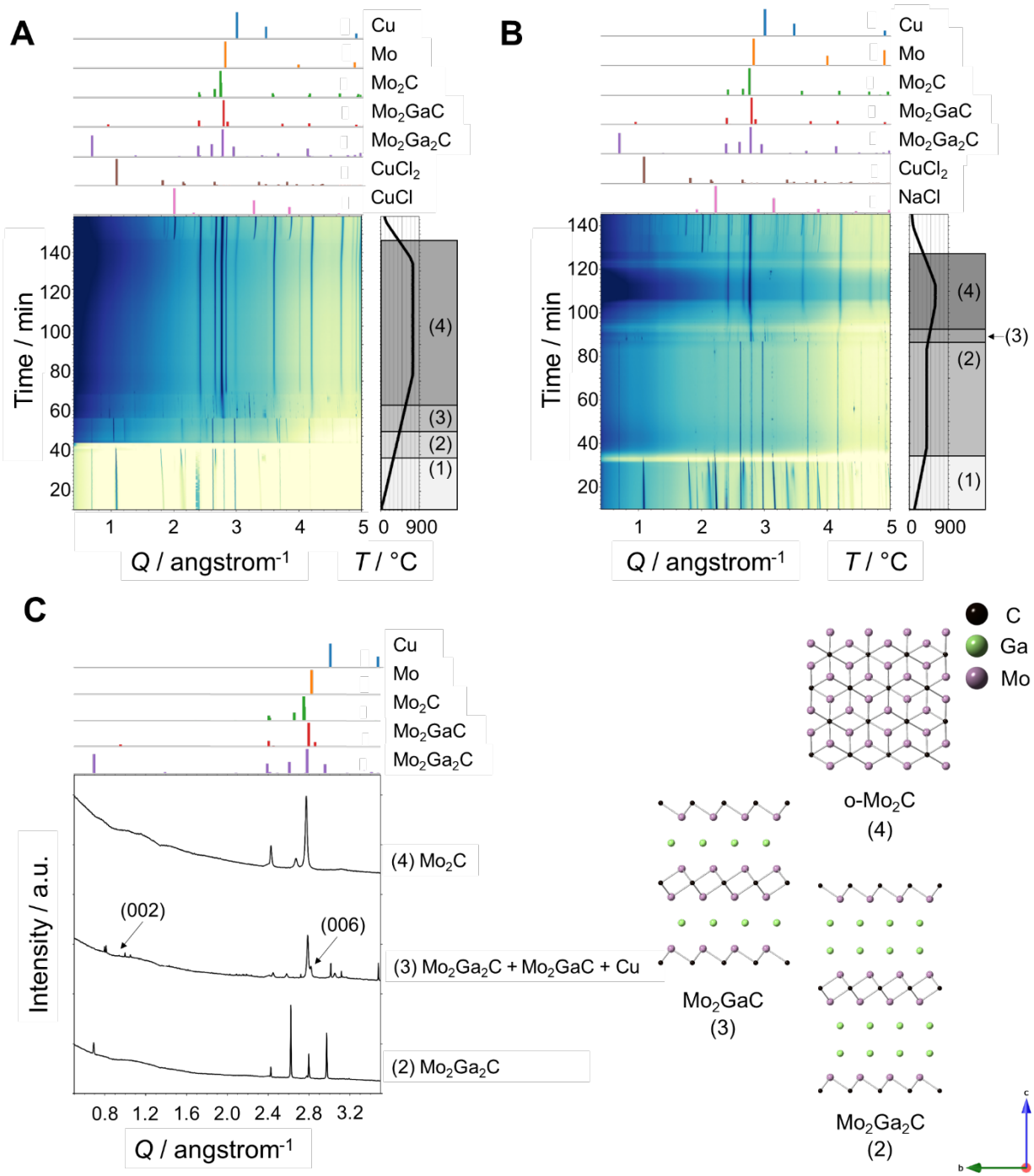

Figure 5. Galvanic reactivity of Mo_2Ga_2C into (A) molten $CuCl_2$ (Mo_2Ga_2C:$CuCl_2$ ratio 1:6 at.) and into (B) a molten mixture $CuCl_2$:NaCl, with Mo_2Ga_2C:$CuCl_2$:NaCl ratio 1:6:9 at. *In situ* XRD patterns are displayed as heatmaps with corresponding measured temperature profiles. The room temperature reference patterns are displayed on top of the heatmaps. (C) XRD patterns corresponding to the main selected area of the map displayed in (B), with schemes of the crystal structures corresponding to the different temperature zones.

***In situ* XRD in strongly oxidizing molten salts.** We discuss first the thermal treatment of Mo_2Ga_2C in molten $CuCl_2$, a highly oxidizing medium, by maintaining a large excess of oxidizing species (Mo_2Ga_2C:$CuCl_2$ ratio of 1:6 mol.). The XRD patterns (**Figure 5A**, details in **Figures S4 and S5**) were recorded during heating at 10 °C min^{-1} from room temperature to 750 °C, then a temperature plateau of 1h. Four steps were identified. In step 1, characteristic peaks of $CuCl_2$ and Mo_2Ga_2C are observed at room temperature, until melting of the salt at 370 °C where the peaks of $CuCl_2$ start to disappear, and the diffuse scattering of the molten salt is observed. Then, in step (2),Mo_2Ga_2C is maintained, presumably dispersed in the molten salt. Some $CuCl_2$ remains crystalline. A peak at 1.2 $Å^{-1}$ could not be indexed. At 517 °C, $CuCl_2$ is decomposed into CuCl, which is fully melt at the end of step (3) at 650 °C. These observations are consistent with the reported behaviour of $CuCl_2$ and CuCl.[22] During step (3), Cu is also detected with its (111) and (002) reflections at 3.0 and 3.5 $Å^{-1}$. The formation of Cu further supports a galvanic reaction. Step (4) begins at 650 °C, where the {1-13}/{103} reflection of Mo_2Ga_2C at 2.65 $Å^{-1}$ disappear while the (102), {200} and (02-1) reflections of orthorhombic Mo_2C at respectively 2.8, 2.7 and 2.45 $Å^{-1}$ appear, thereby demonstrating that Mo_2Ga_2C evolves into orthorhombic Mo_2C, and then that etching occurs. However, no lamellar etched phase could be detected and a peak corresponding to molybdenum appears from 624 °C with the reflections at 2.9 and 4.0 $Å^{-1}$ (step 4). Therefore, the medium is too oxidizing to decipher etching steps and too reactive to avoid destruction of the molybdenum carbide phase. For this reason, we have slowed down the reaction by diluting $CuCl_2$ with a redox-inactive salt, NaCl, and by decreasing the plateau temperature. The XRD patterns recorded with the mixture ratio Mo_2Ga_2C:$CuCl_2$:NaCl of 1:6:9 mol. are displayed in **Figure 5B-C** (details in **Figures S6 and S7**). The salt mixture, observed in step 1, melts at 362 °C. No change of the Mo_2Ga_2C peaks could be detected during the first 40 min of the plateau (step 2). Then, the temperature was further increased (step 3). At 430 °C, peaks emerged at 0.95, 1.87 and 2.85 $Å^{-1}$, which correspond to the (002), (004) and (006) reflections of Mo_2GaC. Meanwhile, the Mo_2Ga_2C (002) peak at 0.7 $Å^{-1}$, disappears (**Figure 5C**). Likewise, peaks indexed to Cu appear at 3.04 and 3.50 $Å^{-1}$ (step 3). However, these peaks disappear during step 4. Indeed, Cu is oxidized by excess $CuCl_2$ into CuCl, which is molten

at this temperature. The formation of CuCl is supported by its {111} peak at 2.05 $Å^{-1}$, which appears during the temperature decrease and the salt recrystallization from 130 min at the end of the experiment. The concomitant formation of copper and Mo_2GaC evidences galvanic etching, in agreement with the metallic state of Ga into Mo_2Ga_2C:[23]

$$Mo_2Ga_2C + 1.5\ CuCl_2 \rightarrow Mo_2GaC + 1.5\ Cu + GaCl_{3\,(g)} \quad (3)$$

The (006) Mo_2GaC peak shifts to lower *Q* values during heating and disappears at 480 °C. This phenomenon is ascribed to the etching of the interleaved Ga in the Mo_2GaC phase, which leads to an increase of the distance between the Mo_2C layers. One can discard thermal dilatation as the origin of the (006) peak shift to low *Q* values, as peaks at 2.45 and 4.2 $Å^{-1}$ corresponding to {1,-1,0}; (0,1,0) ; {1,1,0}, and {2,-1,0} reflections simultaneously shift to high *Q* values, thus indicating a structural transformation, contrary to thermal dilatation that would result most commonly in a shift of all peaks to low *Q* values. At 492 °C, orthorhombic Mo_2C appears and becomes the only phase detected from 546 °C (step 4). Hence, the interleaved Ga from Mo_2GaC is also etched by the molten copper chloride salt:

$$Mo_2GaC + 1.5\ CuCl_2 \rightarrow Mo_2C + 1.5\ Cu + GaCl_{3\,(g)} \quad (4)$$

***In situ* XRD in mildly oxidizing molten salts.** To further decorrelate the sequential etching of the double Ga layers in Mo_2Ga_2C, we have moved to $CoCl_2$, a Lewis acidic salt weaker than $CuCl_2$ (**Figure 1**). We have maintained the same dilution conditions, with a Mo_2Ga_2C:$CoCl_2$:NaCl ratio of 1:6:9 mol. (**Figure 6A, details in Figures S8 to S10**). Step 1 corresponds to the initial mixture until melting of the salt. Step 2 spans the period between melting and the end of the first plateau at 500 °C, while Mo_2Ga_2C is maintained. Further increase of the temperature to 600 °C in step 3 leads to the disappearance of the (002) peak of Mo_2Ga_2C at 0.72 $Å^{-1}$, while we observe a signature of galvanic etching, as characteristic peaks of Co appear at 3.1 and 3.6 $Å^{-1}$. As expected, the galvanic etching was slowed

down, since the (006) Mo_2GaC peak appears at 600 °C at 2.85 $Å^{-1}$ after 4 min of plateau with the disappearance of Mo_2Ga_2C reflections, *versus* 430 °C with the $CuCl_2$:NaCl mixture. However, at the same time, Mo_2C appears. Thus, the 2 reactions below occur:

$$Mo_2Ga_2C + 1.5\ CoCl_2 \rightarrow Mo_2GaC + 1.5\ Co + GaCl_3 \quad (5)$$

$$Mo_2GaC + 1.5\ CoCl_2 \rightarrow Mo_2C + 1.5\ Co + GaCl_3 \quad (6)$$

Several minutes later, Mo_6Co_6C crystallization is detected, which is consistent with reduced Co species. Further increase of the temperature leads to the disappearance of Mo_2GaC at 694 °C, above which Mo_2C, Mo_6Co_6C and Co are the only crystalline phase detected in the reaction mixture. Once $CoCl_2$ is reduced into Co, it reacts with Mo_2C to form Mo_6Co_6C.[24]

***In situ* XAS in mildly oxidizing molten salts.** XANES recorded during the reaction of Mo_2Ga_2C into the molten mixture $CoCl_2$:NaCl (**Figure 6B**) evidences a downward shift of the Co K-edge to low energy, which confirms the reduction of Co^{2+} species from the salt. This trend is consistent with *in situ* XRD and confirms galvanic etching according to equations (5) and (6). It also shows that etching starts early after melting of the salt, as for Ti_3AlC_2.

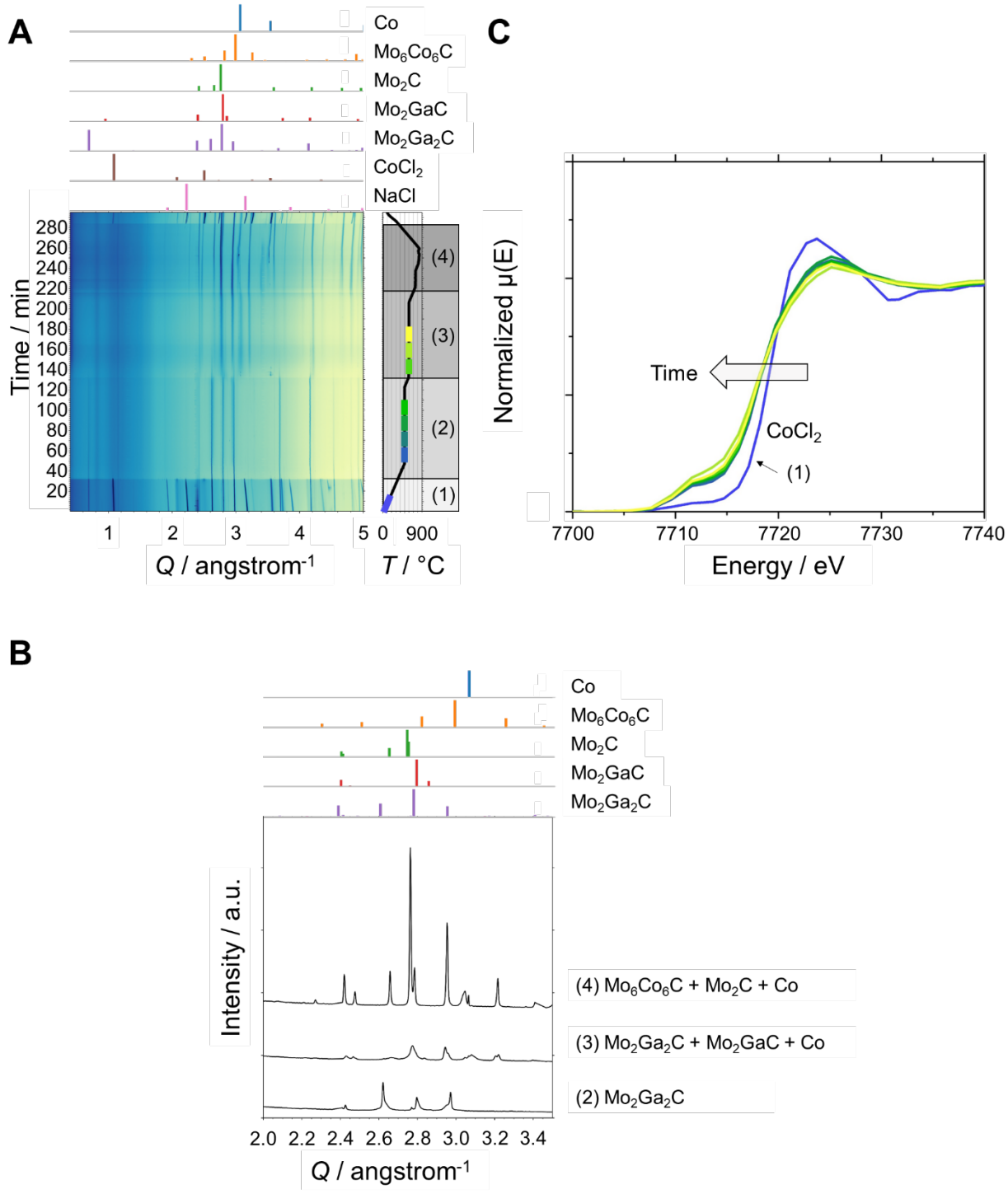

Figure 6. Galvanic reactivity of Mo_2Ga_2C into a molten mixture $CoCl_2$:NaCl, with Mo_2Ga_2C:$CoCl_2$:NaCl ratio 1:6:9 at. (A) *In situ* XRD patterns displayed as a heatmap; corresponding measured temperature profile, and corresponding room temperature reference patterns on the top. Five stages are highlighted in the XRD temperature profile, with identification of the main crystalline phases. (B) XRD patterns corresponding to main selected areas of the map displayed in (A). (C) *In situ* Co K-edge XANES recorded during a similar experiment. The time period for the acquisition of each spectrum is color-

coded on the temperature profile in (A). The spectrum labelled (1) corresponds to the initial state, containing solely $CoCl_2$.

Different galvanic reactivity between Ti_3AlC_2 and Mo_2Ga_2C. Galvanic reactivity of Mo_2Ga_2C into molten salts results in sequential etching of the Ga layers. Contrary to the first step of galvanic reactivity of Ti_3AlC_2, we did not observe any replacement of Ga by metal atoms originating from the reduction of the molten salt cations, Cu or Co. Although in depth calculations would be needed to compare the relative stabilities of MAX phases resulting from galvanic replacement and etching, the results presented herein suggest that MAX-related Mo-Cu/Co-C phases are too unstable to be reached, even through the low temperature molten salts route.

We also did not detect any Cl^--intercalated molybdenum phase, which would have corresponded to the second reactivity step of the titanium aluminum phase to form $Ti_3C_2Cl_2$. This observation might be related to a poorer stability of Mo-C-Cl phases bearing oxidized Mo species, compared to $Ti_3C_2Cl_2$. This hypothesis is supported by the Bader charges calculated from the tabulated crystal structures (**Table 1**). Indeed, Ti is more positively charged than Mo in MAX-related phases (**Table 1**), in agreement with the higher ionization energy of Mo *versus* Ti. Bader charges show that during the transformation from Ti_3ZnC_2 to $Ti_3C_2Cl_2$, Ti atoms on the surface of the carbide layer structural units, linked to Cl^- anions, undergo a strong increase of their charge, as expected from the higher difference in electronegativity between Ti and Cl, compared to Ti and Zn, which is in agreement with reaction (2). For Mo-based phases, all Mo atoms are at the surface of the carbide layers. Binding of Cl^- would trigger a large increase of the Mo partial charge, which is probably less energetically favorable than for Ti phases due to the higher ionization energy of Mo. Besides, we note that stacking of the molybdenum carbide layers in Mo_2GaC results in orthorhombic Mo_2C (see structural schemes in **Figure 5C**). This close structural relationship of the two compounds, combined with the high stability of orthorhombic Mo_2C and the unfavorable binding of Cl^- to Mo atoms, further suggests that etching of the Ga layer in Mo_2GaC results in direct structural transformation into orthorhombic Mo_2C by collapse of the carbide layers.

The contrasted reactivities of Ti- and Mo-based layered compounds related to the MAX crystal structure show that the formation of a halide-terminated MXene by galvanic replacement in molten salts is only possible if the carbide or nitride layer of the MXene is able to undergo oxidation, hence to bear a high positive charge. This agrees with the previous reports on molten salts-driven galvanic replacement in MAX phases, which yielded halide-terminated layers only for Ti, Nb and Ta metals, hence relatively electropositive transition metals.[3,6,8,9,10] If the pristine layers cannot stand such a redox reactivity, we anticipate that compositional and/or structural modifications of these layers may stabilize the halide-terminated MXene. Among the possible tracks, one could consider adjusting either the metal composition by substitution with a second electropositive metal, or the structure by using thicker layers to distribute the positive charge over a larger number of atoms.

Table 1. Atomic Bader charges calculated for the MAX-related Ti- and Mo-based phases.

	M†	A	C	Cl
Ti_3AlC_2	1.64 (layer core)	-0.70	-1.85	
	1.38 (layer surface)			
Ti_3ZnC_2	1.63 (layer core)	-0.77	-1.85	
	1.42 (layer surface)			
$Ti_3C_2Cl_2$	1.62 (layer core)		-1.82	-0.62
	1.63 (layer surface)			
Mo_2Ga_2C	0.75	-0.05	-1.40	
Mo_2GaC	0.83	-0.22	-1.44	

† For Ti-based phases, charges are provided for Ti atoms within the carbide layers ("layer core") and at the surface of the carbide layers ("layer surface"), see structural schemes in **Figure 3B**. Only the Ti atoms from the surface layer are linked to Al, Zn, or Cl. In Mo-based phases, all Mo atoms are at the carbide layer surface.

CONCLUSIONS

The combination of *in situ* XRD and *in situ* XAS highlights the versatility of galvanic reactions in molten salts. We have evidenced fast galvanic replacement consisting in combined etching and intercalation for Ti_3AlC_2 into molten $ZnCl_2$, which can be related to an "unzipping" process known for intercalation

of organic moieties into clays and hybrid materials. The case of Mo_2Ga_2C shows that besides replacement, galvanic etching can also take place, leading to a collapse of the layered structure. which highlights the entanglement between the relative stability of intercalated and etched phases, and suggests the possibility to precisely tune such reactivity with the composition and structure of the parent MAX phases, but also with the composition of the molten salt. Thus, by controlling these parameters in the molten salt process coupled with theoretical calculations, it is reasonable to think that new MXenes or related phases could be synthesized in the near future.

METHODS

Reagents. $CuCl_2$ (99 %, Sigma-Aldrich) and NaCl (99 %, Merck) were used as received. anhydrous $CoCl_2$ (99.7 %, Alfa Aesar) was further treated at 350 °C for 20 h, under vacuum. NaCl (99 %, Merck) and anhydrous $ZnCl_2$ (99.95 %, Alfa Aesar) were treated at 150 °C under vacuum overnight. Ti_3AlC_2 and Mo_2Ga_2C powders were synthesized according to previously reported procedures.[16,17]

Mixtures for *in situ* studies. All reaction mixtures were prepared inside an argon-filled glovebox. Ti_3AlC_2 and $ZnCl_2$ powders were mixed in 1:6 mol. ratio and ground in a mortar. For Mo_2Ga_2C**,** Mo_2Ga_2C, MCl_2 (M= Cu, Co) and NaCl powders were mixed in 1:6:9 mole ratio and mixed with a mortar.

***Ex situ* powder XRD**: XRD patterns of the **figure 2** were carried out with a PANalytical EMPYREAN powder diffractometer using a CuKα radiation source ($K_{\alpha1}$ = 1.5406 Å and $K_{\alpha2}$ = 1.5444 Å) in the Bragg-Brentano θ-θ geometry. XRD patterns were collected between 5 and 145 ° with a 0.026° step and 1200 s dwell time. An ultra-fast X-Ray detector (X'Celerator) was used to collect the signals allowing an important decrease of analysis duration.

***In situ* XRD.** *In situ* X-ray diffraction experiments were carried out at the French SOLEIL Synchrotron facility on the DIFFABS beamline, in transmission mode at an energy (wavelength) of 17.878 keV (0.6935 Å). A double crystal monochromator equipped with two Si(1,1,1) crystals was used to tune the energy. The spot size was size was 220x280 μm^2 (VxH, fwhm). We used a homemade capillary oven

that will be detailed elsewhere. In brief, it enables performing X-ray diffraction *in situ* during controlled heating of the reaction mixture in a 1 mm-diameter quartz capillary opened under argon flow, to mimic the conditions of *ex situ* lab synthesis. For these experiments, we used a circular 2D detector covering 140° detection angle in a single acquisition.[25] The powder was placed in a 1 mm diameter quartz capillary. The capillary was introduced in a sample holder connected to an argon flux and placed in the center of a capillary oven.

The reference crystallographic structures were taken from either the ICSD or the PDF databases: γ-ZnC_2 (PDF #00-030-0572), *δ*-$ZnCl_2$ (PDF #04-005-4434), Ti_3AlC_2 (ICSD #153266), Ti_3ZnC_2 (ICSD #133140), Zn (ICSD #421015), $CuCl_2$ (PDF #00-034-0198), CuCl (PDF #00-006-0344), $CoCl_2$ (ICSD #44398), NaCl (PDF #00-005-0628), Mo_2Ga_2C (ICSD #403577), Mo_2GaC (PDF #00-030-0572), Mo_2C (PDF #01-071-0242), Mo (PDF #00-001-1207), Cu (PDF #00-004-0836), Mo_6Co_6C (PDF #04-005-5151), Co (PDF # 00-015-0806).

For $Ti_3C_2Cl_2$, we have simulated a new XRD patterns with VESTA from the reference ICSD #133145 with the cell parameter c = 11.12 Å corrected to fit data from ref [3].

For the sequential Rietveld refinement during the transformation of Ti_3AlC_2 to Ti_3ZnC_2, cell parameters and crystallite domain sizes were fixed according to refinement of the first pattern of the series. Only the weight fraction of each phase was refined. For each diffractogram, R_{wp} ranged from 4.1 to 6.2 %.

SEM: The morphology of the Mo_2Ga_2C and Ti_3AlC_2 powders was studied using a field emission gun scanning electron microscope (FEG-SEM) 7900F from JEOL.

***In situ* XAS.** The same capillary oven as for *in situ* XRD was used for *in situ* XAS on the same beamline DIFFABS at SOLEIL synchrotron with the same spot size, with an X-ray fluorescence detector positioned on the X-ray entrance side on top of the direct X-ray beam. The energy scales of the spectra recorded at the Zn K and Co K-edges were corrected *versus* the tabulated $ZnCl_2$,[26] and $CoCl_2$, [27] at 9665.0 and 7718.4 eV, respectively.

Bader Charges calculations. Density Functional Theory calculations were performed using the all-electron, full potential augmented-plane-wave (APW) method as implement in the WIEN2k code.[28,29] For all calculations the plane wave basis set was defined using a RKmax of 7.5. The muffin-tin radii associated with the different elements of the materials under consideration were obtained from the automated routine provided with WIEN2k. Exchange and correlation effects were treated in the generalized gradient approximation (GGA) using the Perdew Burk Ernzerhof functional.[30] Unit cell parameters were fixed to their experimental values while considering relaxed atomic positions. The structural models of Brette *et al.*[31] were used for Ti_3AlC_2, $Ti_3C_2Cl_2$ and Mo_2Ga_2C, Mo2GaC unit cell parameters were taken from ref.[32] and those of Ti_3ZnC_2 from ICSD #133140. Sufficient number of *k*-points in the full Brillouin zone were considered, using a Monkhorst-Pack integration, so that further increase would not noticeably change the results. The calculated Bader charge were obtained using the AIM program as implemented in the WIEN2k code.

ASSOCIATED CONTENT

Supporting Information Available: Figures S1 to S3: enlarged *in situ* XRD data for Figure 3. Figures S4 and S5: enlarged *in situ* XRD for Figure 5A. Figures S6 and S7**:** enlarged *in situ* XRD data for Figure 5B. Figures S8 to S10: enlarged *in situ* XRD for Figure 6A.

acknowledgement

This project has received funding from the European Research Council (ERC) Consolidator Grant GENESIS under the European Union's Horizon 2020 research and innovation program (grant agreement n° 864850). The experiments at DIFFABS beamline at Synchrotron SOLEIL have been funded by SOLEIL as the User Proposal 20220509. The Poitiers university co-authors also acknowledge the financial support of the European Union (ERDF), Region Nouvelle Aquitaine and the French government's

“Investissements d’Avenir” program (EUR INTREE, ANR-18-EURE-0010). SC, PC, FB and VM acknowledge financial support from the “Agence National de la Recherche” (reference ANR-18-CE08-014 – MXENECAT project). Computations have been performed on the supercomputer facilities of the “Mésocentre de calcul de Poitou Charentes”.

REFERENCES

(1) Gogotsi, Y.; Huang, Q. MXenes: Two-Dimensional Building Blocks for Future Materials and Devices. *ACS Nano* **2021**, *15* (4), 5775–5780. https://doi.org/10.1021/acsnano.1c03161.

(2) Li, X.; Huang, Z.; Shuck, C. E.; Liang, G.; Gogotsi, Y.; Zhi, C. MXene Chemistry, Electrochemistry and Energy Storage Applications. *Nat. Rev. Chem.* **2022**, *6* (6), 389–404. https://doi.org/10.1038/s41570-022-00384-8.

(3) Li, M.; Lu, J.; Luo, K.; Li, Y.; Chang, K.; Chen, K.; Zhou, J.; Rosen, J.; Hultman, L.; Eklund, P.; Persson, P. O. Å.; Du, S.; Chai, Z.; Huang, Z.; Huang, Q. Element Replacement Approach by Reaction with Lewis Acidic Molten Salts to Synthesize Nanolaminated MAX Phases and MXenes. *J. Am. Chem. Soc.* **2019**, *141* (11), 4730–4737. https://doi.org/10.1021/jacs.9b00574.

(4) Anasori, B.; Lukatskaya, M. R.; Gogotsi, Y. 2D Metal Carbides and Nitrides (MXenes) for Energy Storage. *Nat. Rev. Mater.* **2017**, *2* (2), 16098. https://doi.org/10.1038/natrevmats.2016.98.

(5) Lim, K. R. G.; Shekhirev, M.; Wyatt, B. C.; Anasori, B.; Gogotsi, Y.; Seh, Z. W. Fundamentals of MXene Synthesis. *Nat. Synth.* **2022**, *1* (8), 601–614. https://doi.org/10.1038/s44160-022-00104-6.

(6) Kamysbayev, V.; Filatov, A. S.; Hu, H.; Rui, X.; Lagunas, F.; Wang, D.; Klie, R. F.; Talapin, D. V. Covalent Surface Modifications and Superconductivity of Two-Dimensional Metal Carbide MXenes. *Science* **2020**, *369*, 979–983.

(7) Huang, P.; Han, W.-Q. Recent Advances and Perspectives of Lewis Acidic Etching Route: An Emerging Preparation Strategy for MXenes. *Nano-Micro Lett.* **2023**, *15* (1), 68. https://doi.org/10.1007/s40820-023-01039-z.

(8) Urbankowski, P.; Anasori, B.; Makaryan, T.; Er, D.; Kota, S.; Walsh, P. L.; Zhao, M.; Shenoy, V. B.; Barsoum, M. W.; Gogotsi, Y. Synthesis of Two-Dimensional Titanium Nitride Ti_4N_3 (MXene). *Nanoscale* **2016**, *8* (22), 11385–11391. https://doi.org/10.1039/C6NR02253G.

(9) Li, Y.; Shao, H.; Lin, Z.; Lu, J.; Liu, L.; Duployer, B.; Persson, P. O. Å.; Eklund, P.; Hultman, L.; Li, M.; Chen, K.; Zha, X.-H.; Du, S.; Rozier, P.; Chai, Z.; Raymundo-Piñero, E.; Taberna, P.-L.; Simon, P.; Huang, Q. A General Lewis Acidic Etching Route for Preparing MXenes with Enhanced Electrochemical Performance in Non-Aqueous Electrolyte. *Nat. Mater.* **2020**, *19* (8), 894–899. https://doi.org/10.1038/s41563-020-0657-0.

(10) Liu, L.; Zschiesche, H.; Antonietti, M.; Daffos, B.; Tarakina, N. V.; Gibilaro, M.; Chamelot, P.; Massot, L.; Duployer, B.; Taberna, P.; Simon, P. Tuning the Surface Chemistry of MXene to Improve Energy Storage: Example of Nitrification by Salt Melt. *Adv. Energy Mater.* **2023**, *13* (2), 2202709. https://doi.org/10.1002/aenm.202202709.

(11) Baumler, K. J.; Adams, O. S.; Schaak, R. E. One-Step Topochemical Transformation of MoAlB into Metastable Mo2AlB2 Using a Metal Chloride Salt Reaction. *Chem. Commun.* **2023**, *59* (32), 4814–4817. https://doi.org/10.1039/D3CC00138E.

(12) Shoemaker, D. P.; Hu, Y.-J.; Chung, D. Y.; Halder, G. J.; Chupas, P. J.; Soderholm, L.; Mitchell, J. F.; Kanatzidis, M. G. In Situ Studies of a Platform for Metastable Inorganic Crystal Growth and Materials Discovery. *Proc. Natl. Acad. Sci.* **2014**, *111* (30), 10922–10927. https://doi.org/10.1073/pnas.1406211111.

(13) Zhou, X.; Mandia, D. J.; Park, H.; Balasubramanian, M.; Yu, L.; Wen, J.; Yakovenko, A.; Chung, D. Y.; Kanatzidis, M. G. New Compounds and Phase Selection of Nickel Sulfides via Oxidation State Control in Molten Hydroxides. *J. Am. Chem. Soc.* **2021**, *143* (34), 13646–13654. https://doi.org/10.1021/jacs.1c05107.

(14) Zhou, X.; Kolluru, V. S. C.; Xu, W.; Wang, L.; Chang, T.; Chen, Y.-S.; Yu, L.; Wen, J.; Chan, M. K. Y.; Chung, D. Y.; Kanatzidis, M. G. Discovery of Chalcogenides Structures and Compositions Using Mixed Fluxes. *Nature* **2022**, *612* (7938), 72–77. https://doi.org/10.1038/s41586-022-05307-7.

(15) Igoa Saldaña, F.; Defoy, E.; Janisch, D.; Rousse, G.; Autran, P.-O.; Ghoridi, A.; Séné, A.; Baron, M.; Suescun, L.; Le Godec, Y.; Portehault, D. Revealing the Elusive Structure and Reactivity of Iron Boride α-FeB. *Inorg. Chem.* **2023**, *62* (5), 2073–2082. https://doi.org/10.1021/acs.inorgchem.2c03709.

(16) Benchakar, M.; Loupias, L.; Garnero, C.; Bilyk, T.; Morais, C.; Canaff, C.; Guignard, N.; Morisset, S.; Pazniak, H.; Hurand, S.; Chartier, P.; Pacaud, J.; Mauchamp, V.; Barsoum, M. W.; Habrioux, A.; Célérier, S. One MAX Phase, Different MXenes: A Guideline to Understand the Crucial Role of Etching Conditions on Ti3C2Tx Surface Chemistry. *Appl. Surf. Sci.* **2020**, *530*, 147209. https://doi.org/10.1016/j.apsusc.2020.147209.

(17) Benchakar, M.; Natu, V.; Elmelegy, T. A.; Sokol, M.; Snyder, J.; Comminges, C.; Morais, C.; Célérier, S.; Habrioux, A.; Barsoum, M. W. On a Two-Dimensional MoS2/Mo2CTx Hydrogen Evolution Catalyst Obtained by the Topotactic Sulfurization of Mo2CTx MXene. *J. Electrochem. Soc.* **2020**, *167* (12), 124507. https://doi.org/10.1149/1945-7111/abad6e.

(18) Fillaux, C. Etude Structurale et Vibrationnelle Du Chlorure de Zinc à Hautes Pressions et Hautes Températures. These de doctorat, Paris 6, 2004. https://www.theses.fr/2004PA066536 (accessed 2023-05-25).

(19) Divins, N. J.; Kordus, D.; Timoshenko, J.; Sinev, I.; Zegkinoglou, I.; Bergmann, A.; Chee, S. W.; Widrinna, S.; Karslıoğlu, O.; Mistry, H.; Lopez Luna, M.; Zhong, J. Q.; Hoffman, A. S.; Boubnov, A.; Boscoboinik, J. A.; Heggen, M.; Dunin-Borkowski, R. E.; Bare, S. R.; Cuenya, B. R. Operando High-Pressure Investigation of Size-Controlled CuZn Catalysts for the Methanol Synthesis Reaction. *Nat. Commun.* **2021**, *12* (1), 1435. https://doi.org/10.1038/s41467-021-21604-7.

(20) Andreou, F. T.; Barylska, B.; Ciesielska, Z.; Szczerba, M.; Derkowski, A.; Gionis, V.; Siranidi, E.; Chryssikos, G. D. Intercalation of N-Methylformamide in Kaolinite: In Situ Monitoring by near-Infrared Spectroscopy and X-Ray Diffraction. *Appl. Clay Sci.* **2021**, *212*, 106209. https://doi.org/10.1016/j.clay.2021.106209.

(21) Fernandes, F. M.; Baradari, H.; Sanchez, C. Integrative Strategies to Hybrid Lamellar Compounds: An Integration Challenge. *Appl. Clay Sci.* **2014**, *100*, 2–21. https://doi.org/10.1016/j.clay.2014.05.013.

(22) Zhou, S.; Shen, S.; Zhao, D.; Zhang, Z.; Yan, S. Evaporation and Decomposition of Eutectics of Cupric Chloride and Sodium Chloride. *J. Therm. Anal. Calorim.* **2017**, *129* (3), 1445–1452. https://doi.org/10.1007/s10973-017-6360-y.

(23) Lai, C.-C.; Meshkian, R.; Dahlqvist, M.; Lu, J.; Näslund, L.-Å.; Rivin, O.; Caspi, E. N.; Ozeri, O.; Hultman, L.; Eklund, P.; Barsoum, M. W.; Rosen, J. Structural and Chemical Determination of the New Nanolaminated Carbide Mo2Ga2C from First Principles and Materials Analysis. *Acta Mater.* **2015**, *99*, 157–164. https://doi.org/10.1016/j.actamat.2015.07.063.

(24) Wang, S.; Cao, Y.; Jia, W.; Lu, Z.; Jia, D. A Cage-Confinement Strategy to Fabricate Pt-Mo6Co6C Heterojunction for Highly Efficient PH-Universal Hydrogen Evolution. *Appl. Catal. B Environ.* **2021**, *298*, 120579. https://doi.org/10.1016/j.apcatb.2021.120579.

(25) Desjardins, K.; Mocuta, C.; Dawiec, A.; Réguer, S.; Joly, P.; Dubuisson, J.-M.; Alves, F.; Noureddine, A.; Bompard, F.; Thiaudière, D. The CirPAD, a Circular 1.4 M Hybrid Pixel

Detector Dedicated to X-Ray Diffraction Measurements at Synchrotron SOLEIL. *J. Synchrotron Radiat.* **2022**, *29* (1), 180–193. https://doi.org/10.1107/S1600577521012492.
(26) Griffith, E. K.; Ingall, E. D.; Morton, P. L.; Tavakoli, D. A.; Lai, B. Zinc K-Edge XANES Spectroscopy of Mineral and Organic Standards. *J. Synchrotron Radiat.* **2019**, *26* (4), 1302–1309. https://doi.org/10.1107/S160057751900540X.
(27) Schrapers, P.; Mebs, S.; Goetzl, S.; Hennig, S. E.; Dau, H.; Dobbek, H.; Haumann, M. Axial Ligation and Redox Changes at the Cobalt Ion in Cobalamin Bound to Corrinoid Iron-Sulfur Protein (CoFeSP) or in Solution Characterized by XAS and DFT. *PLOS ONE* **2016**, *11* (7), e0158681. https://doi.org/10.1371/journal.pone.0158681.
(28) Blaha, P.; Schwarz, K.; Madsen, G. K. H.; Kvasnicka, D.; Luitz, J.; Laskowsk, R.; Tran, F.; Marks, L.; Marks, L. *WIEN2k: An Augmented Plane Wave Plus Local Orbitals Program for Calculating Crystal Properties*; Techn. Universitat, 2019.
(29) Blaha, P.; Schwarz, K.; Tran, F.; Laskowski, R.; Madsen, G. K. H.; Marks, L. D. WIEN2k: An APW+lo Program for Calculating the Properties of Solids. *J. Chem. Phys.* **2020**, *152* (7), 074101. https://doi.org/10.1063/1.5143061.
(30) Perdew, J. P.; Burke, K.; Ernzerhof, M. Generalized Gradient Approximation Made Simple. *Phys. Rev. Lett.* **1996**, *77* (18), 3865–3868. https://doi.org/10.1103/PhysRevLett.77.3865.
(31) Brette, F.; Kourati, D.; Paris, M.; Loupias, L.; Célérier, S.; Cabioc'h, T.; Deschamps, M.; Boucher, F.; Mauchamp, V. Assessing the Surface Chemistry of 2D Transition Metal Carbides (MXenes): A Combined Experimental/Theoretical 13C Solid State NMR Approach. *J. Am. Chem. Soc.* **2023**, *145* (7), 4003–4014. https://doi.org/10.1021/jacs.2c11290.
(32) Chaix-Pluchery, O.; Thore, A.; Kota, S.; Halim, J.; Hu, C.; Rosen, J.; Ouisse, T.; Barsoum, M. W. First-Order Raman Scattering in Three-Layered Mo-Based Ternaries: MoAlB, Mo2Ga2C and Mo2GaC. *J. Raman Spectrosc.* **2017**, *48* (5), 631–638. https://doi.org/10.1002/jrs.5087.

Table of Content graphic

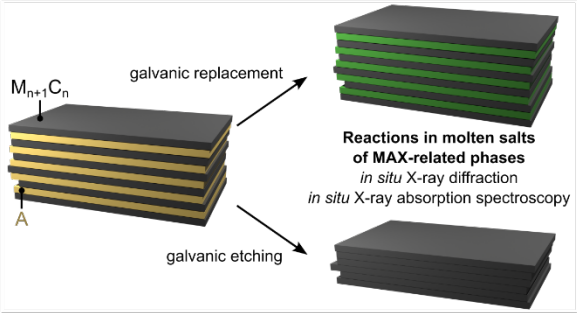

Supplementary information

Galvanic replacement and etching of MAX-related phases in molten salts towards MXenes: an *in situ* study

Emile Defoy,[a] Marzena Baron,[a] Amandine Séné,[a] Anissa Ghoridi,[a] Dominique Thiaudière,[b] Stéphane Célérier,[c] Patrick Chartier,[d] Florian Brette,[d] Vincent Mauchamp,[d] David Portehault[a,*]

[a] Sorbonne Université, CNRS, Laboratoire de Chimie de la Matière Condensée de Paris (CMCP), 4 place Jussieu, F-75005, Paris, France

[b] Synchrotron SOLEIL, L'Orme des Merisiers, Saint-Aubin, 91191 Gif-sur-Yvette, France

[c] Université de Poitiers, CNRS, Institut de Chimie des Milieux et Matériaux de Poitiers (IC2MP), F-86073 Poitiers, France

[d] Institute Pprime, UPR 3346 CNRS, ISAE-ENSMA, Université de Poitiers, BP 30179, 86962 Cedex Futuroscope-Chasseneuil, France

Corresponding author: david.portehault@sorbonne-universite.fr

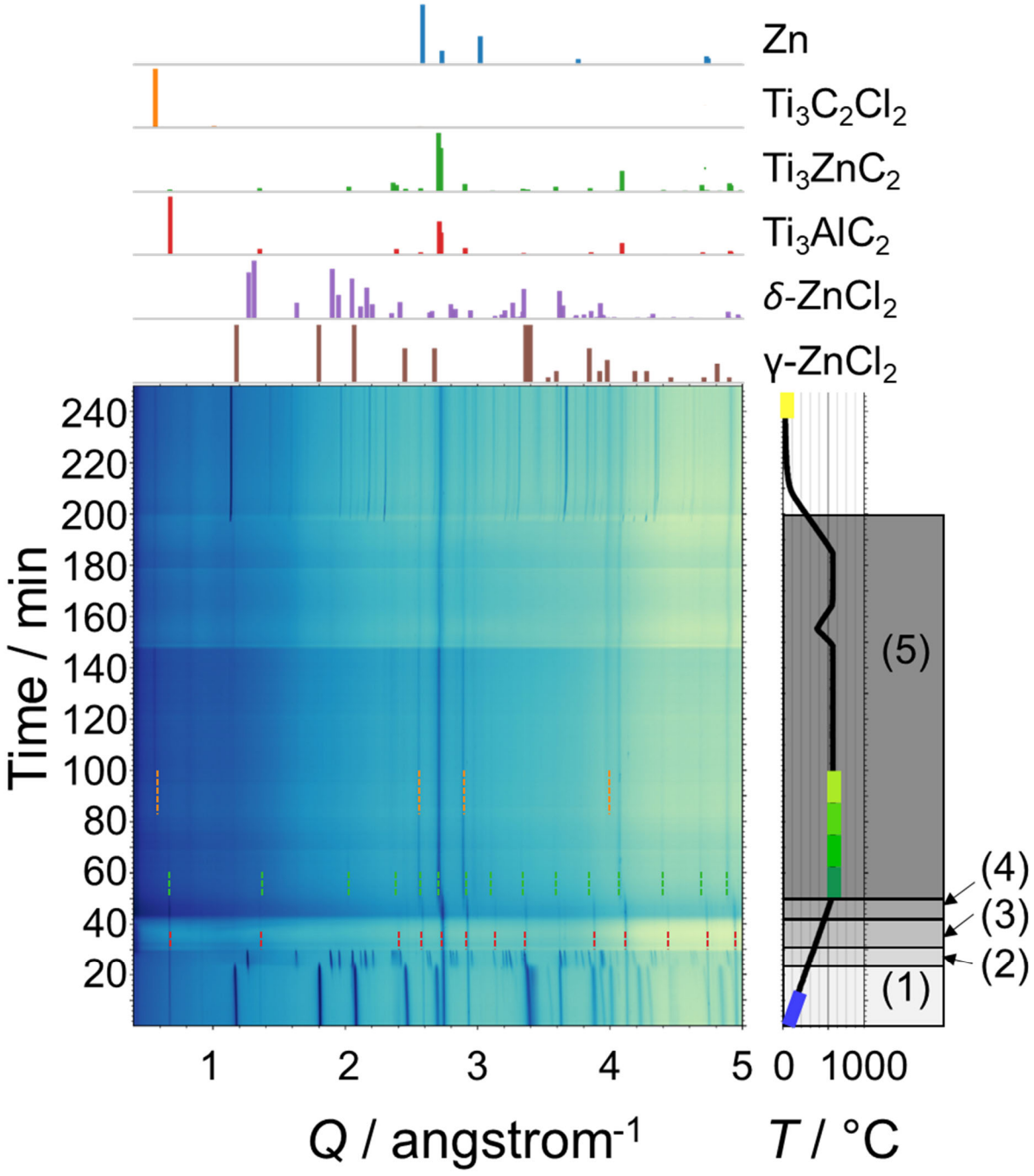

Figure S1. Galvanic reactivity of Ti_3AlC_2 into molten $ZnCl_2$- Enlargement of Figure 3A: *In situ* XRD patterns displayed as a heatmap; corresponding measured temperature profile on the right, and corresponding room temperature reference patterns on the top. The five stages discussed in the main text are highlighted in the XRD temperature profile, with identification of the main crystalline phases.

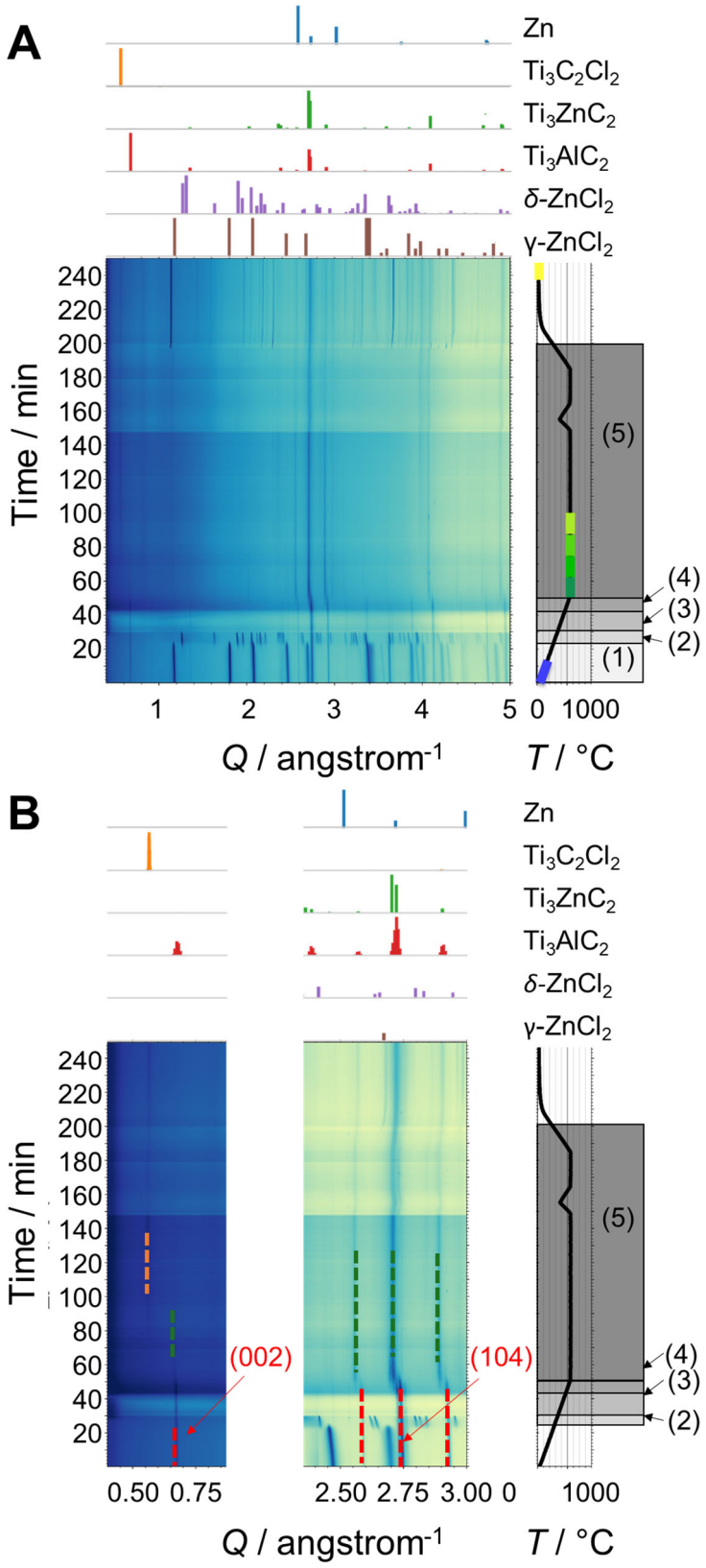

Figure S2. Galvanic reactivity of Ti_3AlC_2 into molten $ZnCl_2$. (A) *In situ* XRD patterns displayed as a heatmap (same as **Figure 3A** and **Figure S1**); corresponding measured temperature profile on the right, and corresponding room temperature reference patterns on the top. The five stages discussed in the text are highlighted in the XRD temperature profile, with identification of the main crystalline phases. (B) Zooms in selected areas of the map displayed in (A).

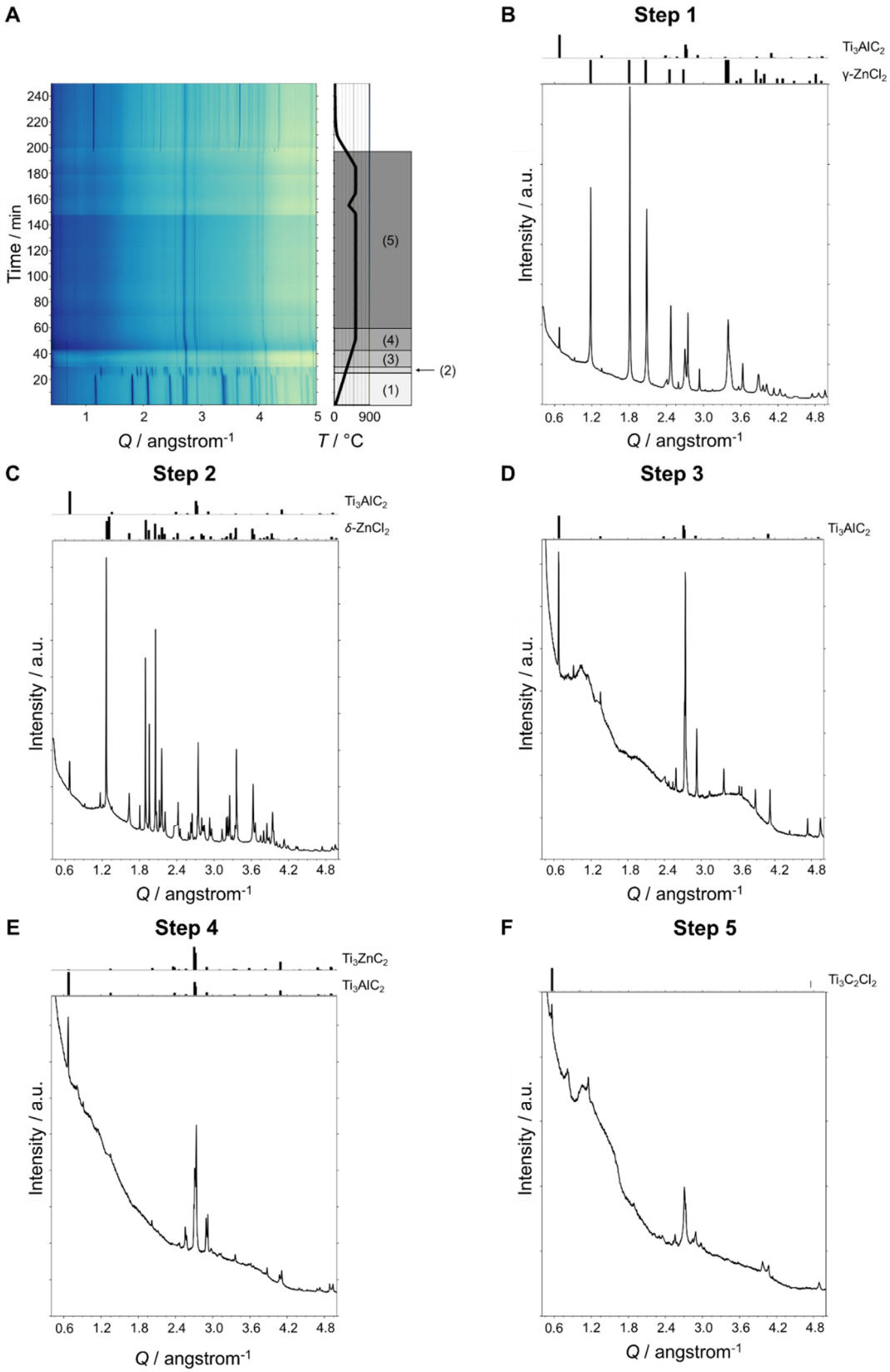

Figure S3. Galvanic reactivity of Ti_3AlC_2 into molten $ZnCl_2$-(A) *In situ* XRD patterns displayed as a heatmap; corresponding measured temperature profile on the right. The five stages discussed in the main text are highlighted in the XRD temperature profile. (B-F) XRD patterns of each step displayed in (A) and in **Figure 3B**, with corresponding room temperature reference patterns of the main phases identified on the top.

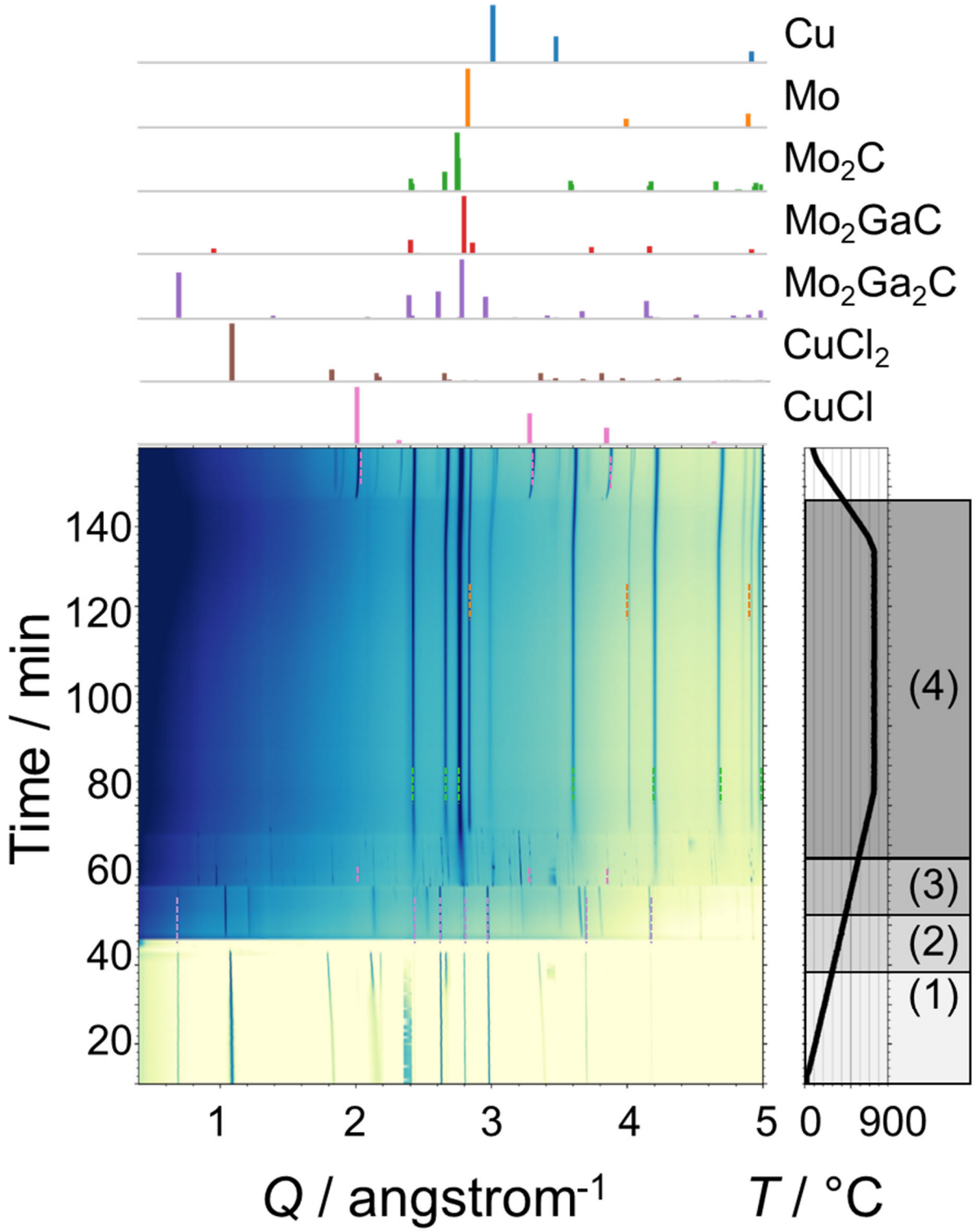

Figure S4. Galvanic reactivity of Mo_2Ga_2C into molten $CuCl_2$ (Mo_2Ga_2C:$CuCl_2$ ratio 1:6 at.) corresponding to Figure 5A. *In situ* XRD patterns are displayed as heatmaps with corresponding measured temperature profiles. The room temperature reference patterns are displayed on top of the heatmaps.

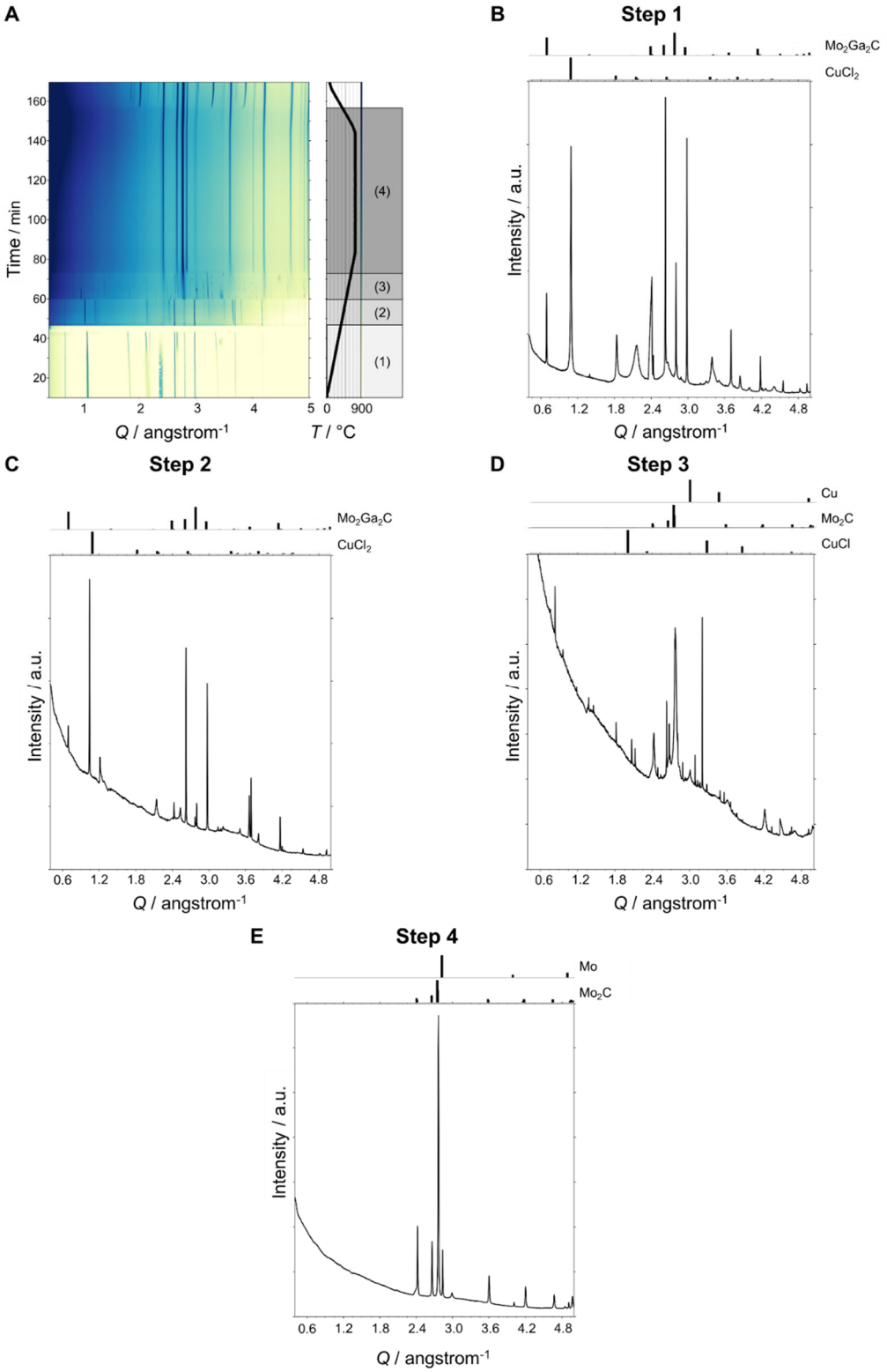

Figure S5. Galvanic reactivity of Mo_2Ga_2C into molten $CuCl_2$ (Mo_2Ga_2C:$CuCl_2$ ratio 1:6 at.) corresponding to Figure 5A.: (A) *In situ* XRD patterns displayed as a heatmap; corresponding measured temperature profile on the right. The four stages discussed in the main text are highlighted in the XRD temperature profile. (B-E) XRD patterns of each step displayed in (A) with corresponding room temperature reference patterns of the main phases identified on the top.

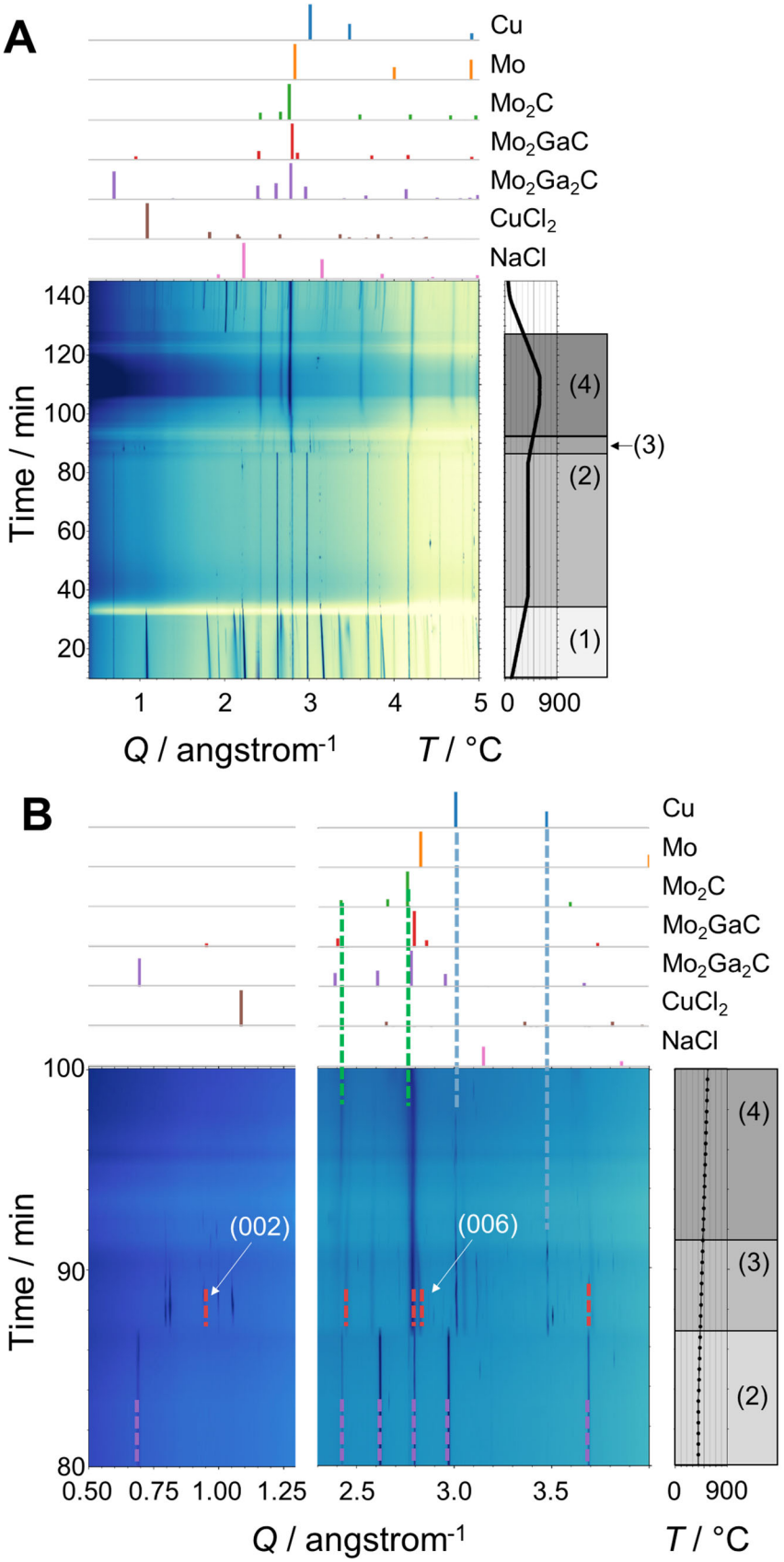

Figure S6. Galvanic reactivity of Mo_2Ga_2C into a molten mixture $CuCl_2$:NaCl, with Mo_2Ga_2C:$CuCl_2$:NaCl ratio 1:6:9 at. (A) *In situ* XRD patterns displayed as heatmaps with corresponding measured temperature profiles. The room temperature reference patterns are displayed on top of the heatmaps. (B) Zooms in selected areas of the map displayed in (A).

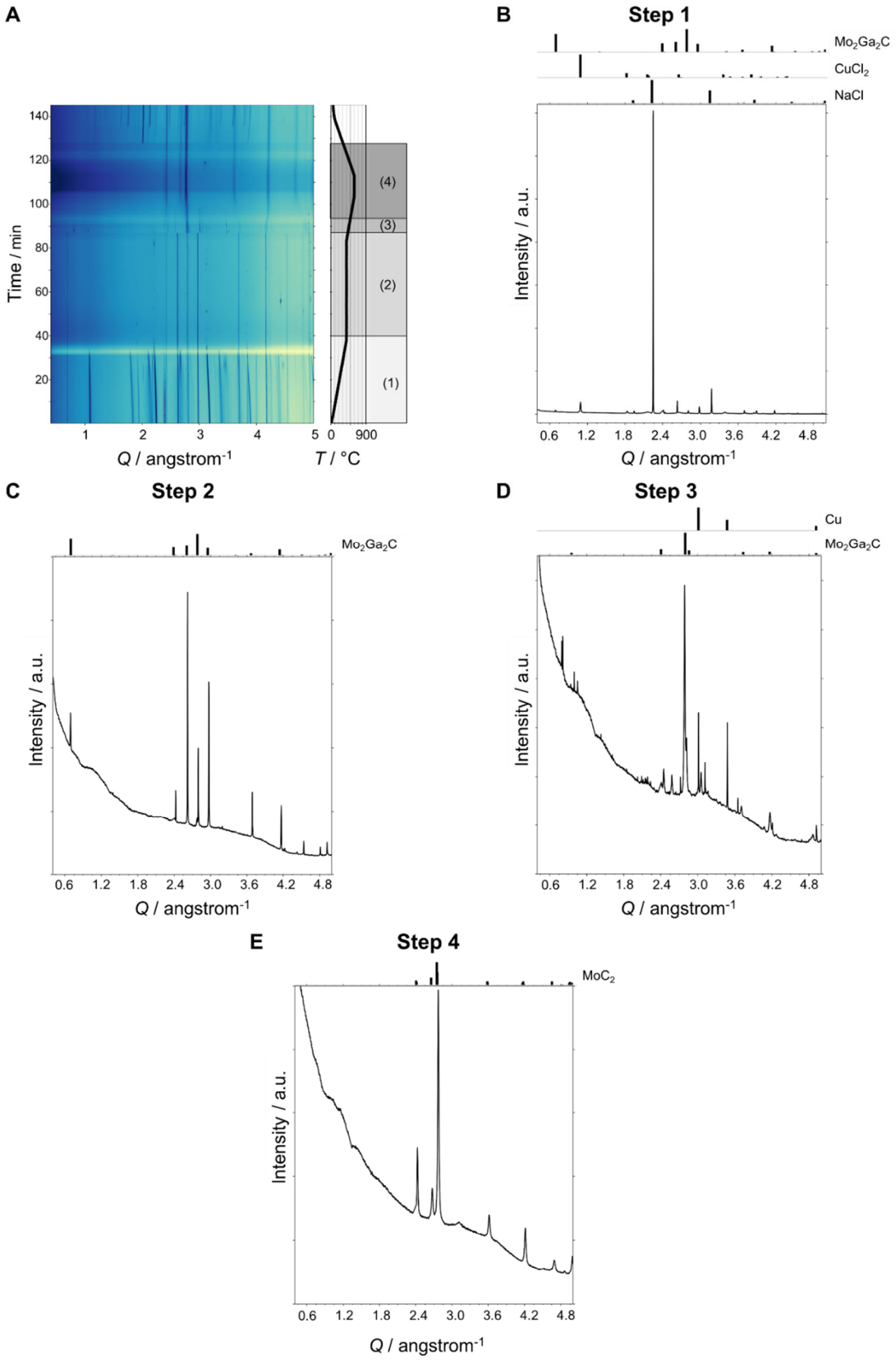

Figure S7. Galvanic reactivity of Mo_2Ga_2C into a molten mixture $CuCl_2$:NaCl, with Mo_2Ga_2C:$CuCl_2$:NaCl ratio 1:6:9 at. (A) *In situ* XRD patterns displayed as a heatmap; corresponding measured temperature profile on the right. The four stages discussed in the main text are highlighted in the XRD temperature profile. (B-E) XRD patterns of each step displayed in (A) with corresponding room temperature reference patterns of the main phases identified on the top.

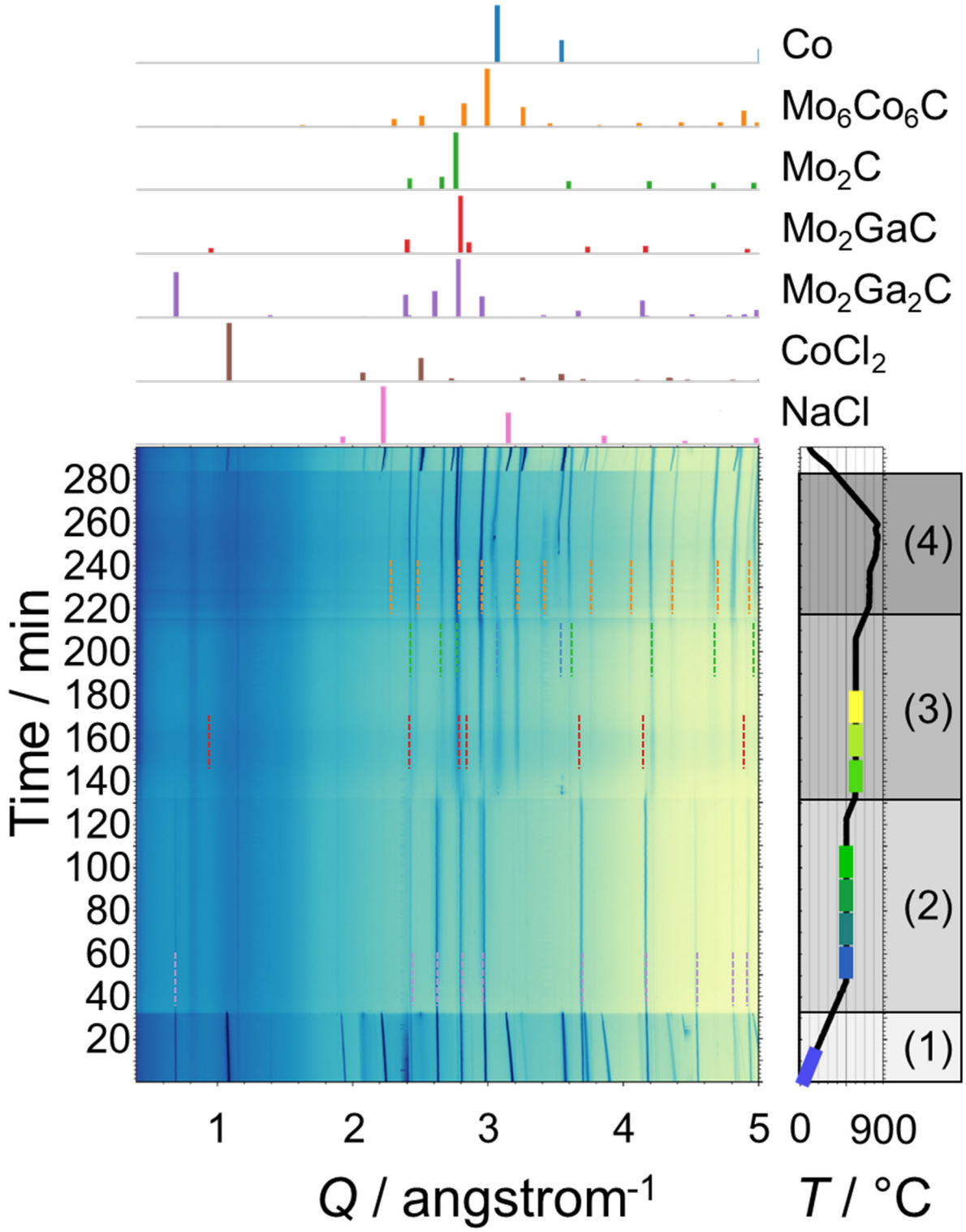

Figure S8. Galvanic reactivity of Mo_2Ga_2C into a molten mixture $CoCl_2$:NaCl, with Mo_2Ga_2C:$CoCl_2$:NaCl ratio 1:6:9 at. *In situ* XRD patterns displayed as a heatmap; corresponding measured temperature profile, and corresponding room temperature reference patterns on the top. Five stages are highlighted in the XRD temperature profile, with identification of the main crystalline phases.

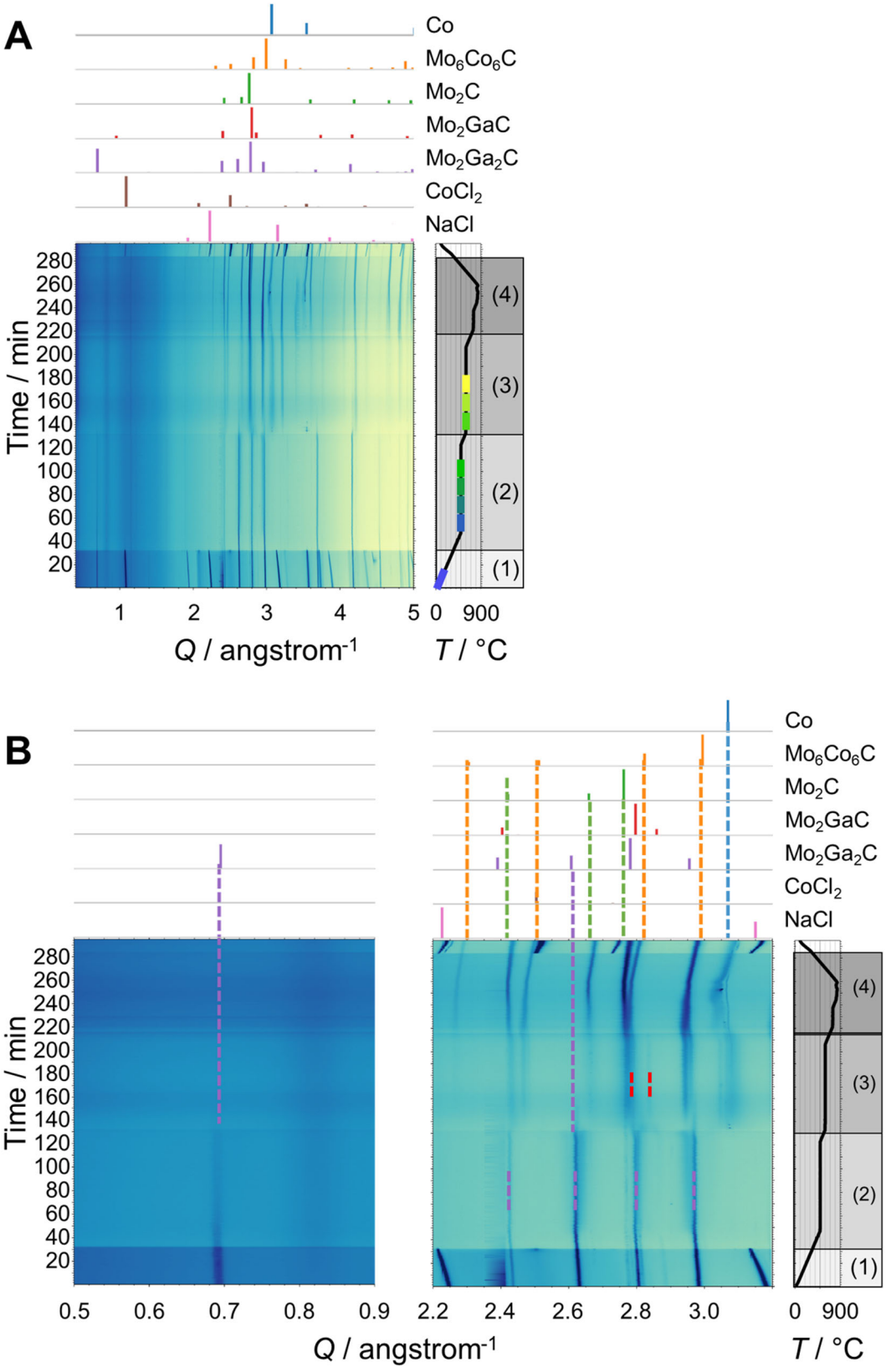

Figure S9. Galvanic reactivity of Mo_2Ga_2C into a molten mixture $CoCl_2$:NaCl, with Mo_2Ga_2C:$CoCl_2$:NaCl ratio 1:6:9 at. *In situ* XRD patterns displayed as a heatmap; corresponding measured temperature profile, and corresponding room temperature reference patterns on the top. Five stages are highlighted in the XRD temperature profile, with identification of the main crystalline phases. (B) Zooms in selected areas of the map displayed in (A).

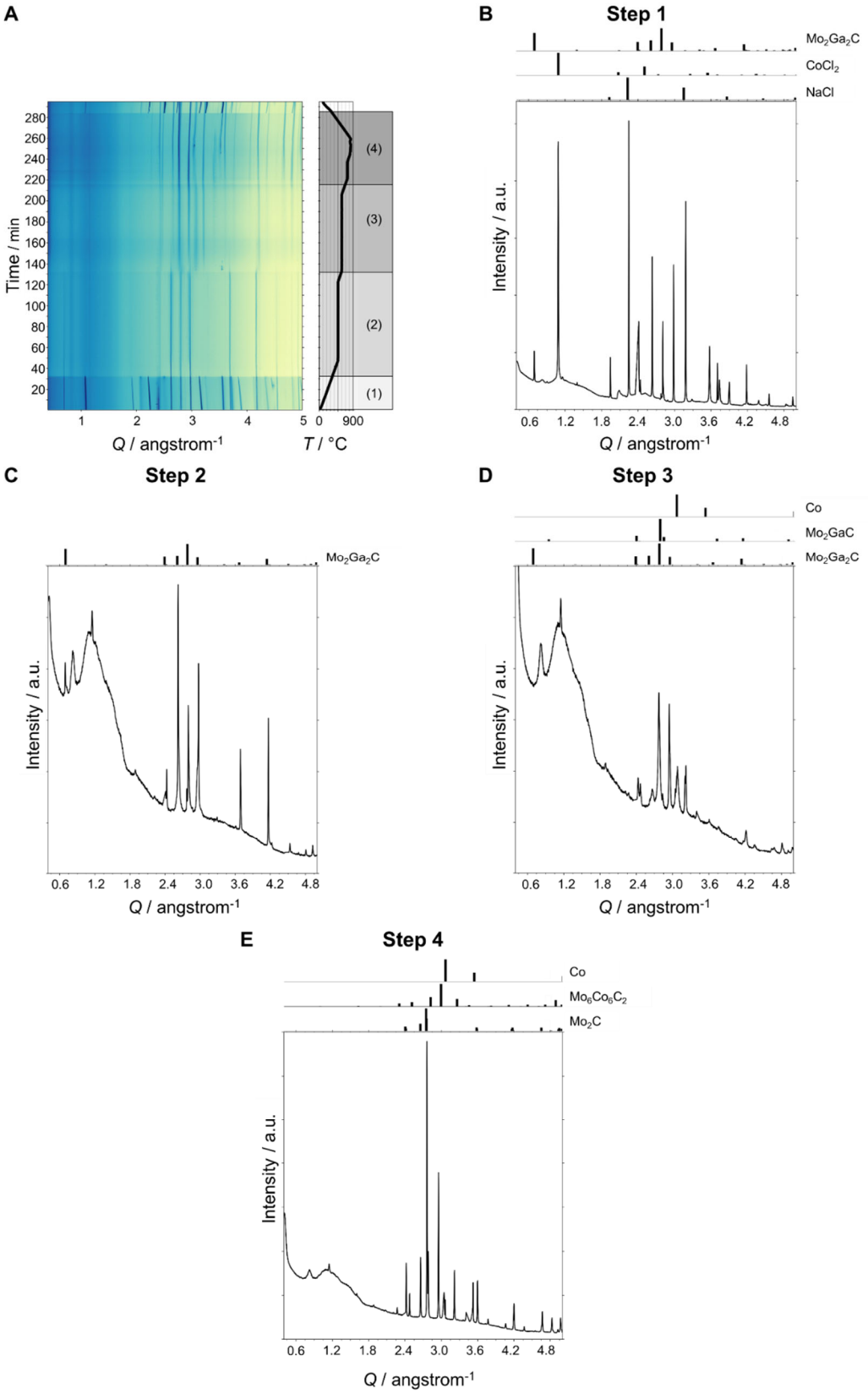

Figure S10. Galvanic reactivity of Mo_2Ga_2C into a molten mixture $CoCl_2$:NaCl, with Mo_2Ga_2C:$CoCl_2$:NaCl ratio 1:6:9 at. (A) *In situ* XRD patterns displayed as a heatmap; corresponding measured temperature profile on the right. The four stages discussed in the main text are highlighted in the XRD temperature profile. (B-E) XRD patterns of each step displayed in (A) with corresponding room temperature reference patterns of the main phases identified on the top.